Contributions to Mineralogy and Petrology (2023) 178:73
https://doi.org/10.1007/s00410-023-02052-6

ORIGINAL PAPER

The origin of Na-alkaline lavas revisited: new constraints from experimental melting of amphibole-rich metasomes+lherzolite at uppermost mantle pressure

Tobias Grützner[1,2,3] · Dejan Prelević[4,5] · Jasper Berndt[3] · Stephan Klemme[3]

Received: 20 January 2023 / Accepted: 30 August 2023 / Published online: 23 September 2023

Abstract

We present a new experimental dataset for reaction experiments between natural amphibole-clinopyroxene metasomes (hornblendite) and synthetic lherzolite that produced Na-rich alkaline melts. Experiments were conducted at 1, 3 and 4 GPa and 1000–1300 °C. The generated melts range from foidite over basanite to phonotephrite. At 1 GPa between 1000 and 1100 °C amphibole decompression-breakdown products generate a phonotephritic melt. Among the breakdown components rhönite was found to be stable up to 1100 °C and 1 GPa. At 3 and 4 GPa the melt compositions are affected by phlogopite melting and shift to more foiditic compositions. We find that the melting of hornblendites and the reaction of the melt with the lherzolite produce wehrlitic residues with different olivine/clinopyroxene ratios. Wehrlite formation does not always require separate metasomatic processes but can be a direct by-product of alkaline volcanism. We applied a metasome melting model to the magmas of the Kula volcanic province, Turkey, and show that at 1 GPa basanite melts and phonotephrite melts cover the whole range of known Kula lava compositions. The Kula lava compositional trend can be therefore generated by basanite-phonotephrite melt mixing. A comparison of high-pressure (3–4 GPa) melts with natural nephelinite data shows overlap with many major, minor, and trace elements but differences in SiO_2, FeO, and TiO_2 argue that the natural nephelinite data do not represent primary metasome melts.

Keywords Alkaline volcanism · Experimental petrology · Kaersutite · Kula volcanic province · Hornblendite · Mantle metasomatism · Wehrlitization

Communicated by Othmar Müntener.

✉ Tobias Grützner
tobias.gruetzner@outlook.com

Dejan Prelević
prelevic@uni-mainz.de

Jasper Berndt
jberndt@wwu.de

Stephan Klemme
stephan.klemme@wwu.de

[1] Institut Für Geowissenschaften, Goethe-Universität Frankfurt, Frankfurt am Main, Germany

[2] Research School of Earth Sciences, Australian National University, Canberra, Australia

[3] Institut Für Mineralogie, Universität Münster, Münster, Germany

[4] Faculty of Mining and Geology, University of Belgrade, Belgrade, Serbia

[5] Institut Für Geowissenschaften, Johannes Gutenberg-Universität Mainz, Mainz, Germany

Introduction

A simplified view suggests that basaltic magmas sourced within the upper mantle are generated by the melting of a homogenous peridotite dominated by olivine. However, since the 1960s numerous papers have been published on the isotopic and trace-elemental composition of mantle-derived basalts, including K- and Na-alkaline ones, suggesting that the mantle is compositionally much more heterogeneous than previously anticipated (e.g. Allègre 1982; Hofmann 1997; Hofmann and White 1982; Zindler and Hart 1986). An alternative to the homogeneous mantle paradigm is the melting of hydrous heterogeneous mantle rocks that contain the so-called hydrous "metasomes" (Foley 1992; Pilet 2015; Pilet et al. 2008). The concepts of melting of heterogeneous, mixed source regions were first introduced to explain the origin of alkaline rocks (Foley 1992; Pilet et al. 2008), but then have been applied to more common rock types, such as ocean island basalts (Pilet 2015), mid-ocean ridge basalts

(Hirschmann and Stolper 1996) and arc-basalts (Straub et al. 2008).

The metasomes comprise different olivine-poor mineral assemblages, with the dominant presence of hydrous minerals like mica, amphibole, or apatite. A large body of evidence support their existence in the mantle and involvement in the source of various mantle-derived rocks: (hydrous) metasomes have been observed as xenoliths in mantle-derived melts (e.g. Nixon 1987) and their discovery has underscored the well-known concept of mantle metasomatism (Frey and Green 1974, Menzies et al. 1987); trace element signatures of olivine phenocrysts indicate the presence of non-peridotite material in the source (Prelević et al. 2013); the LLAMA model (Laminated Lithologies and Aligned Melt Arrays; (Anderson 2011), using high-resolution body wave tomography, supports a strongly metasomatized base of the lithosphere in which these hydrous metasomes are segregated into lamellae.

The melting of hydrous mantle lithologies has been proposed to explain the origin of Na-alkaline lavas occurring in continental and oceanic areas (e.g., Pilet 2015). In both geological settings, a traditional view from the early seventies that these lavas are produced by a small degree of partial melting of a peridotitic mantle source (Hart 1971) has been radically changed after discovering that the trace element and isotopic signatures of high Na/K alkaline basalts from intraplate continental and oceanic settings imply derivation from a source that is more enriched than a MORB depleted mantle. Moreover, the compositional continuum in terms of SiO_2 and alkalis from nephelinites and basanites to alkali olivine basalts and tholeiites universally observed in many intraplate volcanoes that have been interpreted as an increase in the degree of partial melting of a common mantle source (Wilson et al. 1995), has never been reproduced in experiments on mantle lithologies (Pilet 2015), pointing again toward special source conditions for the alkaline lavas. Several models are proposed for this enrichment, including partial melting of similar volatile-present mantle sources under analogous pressure and temperature conditions (Dasgupta and Hirschmann 2007; Dasgupta et al. 2007; Hirose 1997), recycling of oceanic lithosphere into the Earth's convecting mantle with subsequent transformation into pyroxenitic/eclogitic lithologies (Hirschmann et al. 2003; Kogiso et al. 2003; Mallik and Dasgupta 2012), as well as metasomatized mantle enrichment including the formation of volatile-bearing veins in oceanic and continental mantle lithosphere (Halliday et al. 1995; Niu and O'Hara 2003; Pilet 2015; Pilet et al. 2008).

In our experimental study, we simulate melting processes at 1, 3, and 4 GPa within the veined metasomatized mantle. We combine synthetic lherzolite with a natural amphibole-rich metasome, in which these rock types make up two halves of each capsule, to systematically monitor the effects of the P–T change on the major and trace element compositions of the melt infiltrating the peridotite. By augmenting existing data published at pressures of 1.5 GPa (Pilet et al. 2008), we produced an extensive set of high-quality major and trace element dataset that constrains the melt compositions derived from hydrous mixed mantle material at different depths, simulating metasome-rich mantle melting in both young and thin orogenic mantle as well as in the thick off-cratonic lithosphere. Finally, we test the experimental data in two case studies: (1) the 1 GPa experiments are compared to the alkaline rocks of the Kula volcanic province, Turkey, (2) and the 3 and 4 GPa experiments are compared to a large dataset of nephelinites from the GEOROC database.

Methods

Starting material

As starting material, we used mixtures of synthetic lherzolite KLB-1 (Takahashi 1986) and natural amphibole-clinopyroxene-rich metasome from the Kula volcanic Province, Turkey. This metasome could be also referred to as diopside-hornblendite. The Kula metasome samples are coarse-grained sub-rounded amphibole- and clinopyroxene-rich nodules of up to 10 cm in size. Several samples were collected from a basanitic lava flow. The nodules vary slightly in their mineral proportions and are described in detail in Grützner et al. (2013). Sample 10KulX-01 was the largest sample found, has a high amphibole content (about 63 wt.% mass fraction, 23 wt.% clinopyroxene and 15 wt.% olivine), and was therefore chosen as starting material for this experimental study. Its bulk rock composition is very similar to the clinopyroxene-hornblendite from the French Pyrenees (Pilet et al. 2008), except that the Kula sample has higher MgO (18.5 vs. 12.5 wt.%) and lower CaO (12.7 vs. 17.1 wt.%) concentrations than the hornblendite from the Pyrenees. A larger variety of nodules from Kula have been collected and recently described by Şen et al. (2023) including also clinopyroxenites and wehrlites. Their hornblendite and clinopyroxene-hornblendite samples match well with the findings from Grützner et al. (2013). The metasome starting material was ground to a fine-grained powder for about 45 min in an automatic agate ball mill. The lherzolite starting material was prepared from analytical grade oxides and carbonates. To decarbonate the carbonates and to release unwanted hydroxides, MgO, $CaCO_3$, Na_2CO_3, and K_2CO_3 were fired in a Pt-crucible to 1000 °C for at least 2 h, and

were subsequently stored in a drying oven at 110 °C. No trace elements were added to the peridotite starting material. All trace elements that are analyzed in the samples hence derive from the metasome starting material. The starting material compositions are listed in Table 1, natural clinopyroxenes from Kula metasomes are listed in Table 2, amphibole, and rhönite samples in Table 3.

Experimental techniques

Experiments were conducted at the Institute for Mineralogy, Münster University. The starting materials were loaded into Au–Pd capsules in two layers, with the lherzolite layer situated above the metasome. Both lithologies were loaded in a 1:1 wt.% ratio. Experiments at 1 GPa were conducted in a Bristol-type end-loaded piston-cylinder apparatus using a ½" talc-pyrex piston-cylinder assembly with a straight graphite heater. Experiments at 3 and 4 GPa were performed in a 1000-ton Walker-type multi-anvil apparatus using a 14/8 multi-anvil assembly that consists of Cr-bearing MgO octahedra (Mino Ceramic Co, Japan), a graphite heater and pyrophyllite gaskets (Wonderstone Ltd, South Africa). Temperatures were monitored with $W_{97}Re_3$-$W_{75}Re_{25}$ thermocouples and controlled by a Eurotherm controller (Schneider Electric, Germany). The experimental run durations ranged from 20 to 42 h. For a more detailed description of the experimental methods for piston-cylinder and multi-anvil apparatus refer to Grützner et al. (2017). Experimental run conditions for all experiments can be found in Table 4.

To characterize the trace element composition of the natural metasome glasses of this metasome starting material were synthesized with a home-built iridium strip heater (Fedorowich et al. 1993; Stoll et al. 2008). The rock powder was heated to 1500 or 1600 °C on the strip heater and quenched to a homogenous glass within a few seconds. Small glass chips of the USGS reference material BCR-2G were also produced using the strip heater and analyses show a slight Cr_2O_3 loss of both the metasome and the reference glasses that were heated to 1600 °C where Cr is very volatile (Klemme et al. 2022). The glasses produced at 1500 °C show no Cr loss. Therefore, metasome glasses heated up to 1500 °C were used for further analyses. Major elemental oxide concentrations are in excellent agreement with X-ray fluorescence spectrometry data from the same batch of material analyzed by Grützner et al. (2013). The glass composition is listed in Table 5.

Analytical techniques

Qualitative and quantitative analyses of the samples were performed at the Institute for Mineralogy, Münster University. Experimental run products were first characterized by optical microscopy, followed by a JEOL 6510LA scanning electron microscope. Quantitative electron microprobe analyses were performed using a JEOL JXA 8530F field emission electron microprobe (EPMA). Operating conditions were 15 kV accelerating voltage and a beam current of 15 nA for the analyses of the micas, silicates and melt with beam diameters of 2–10 µm, peak counting times between 7 s (Na, K) and 10 s. (Mg, Al, Si, Ca, Ti, Cr, Mn, Fe), and 3 to 5 s on the background, respectively. A set of natural and synthetic standards were used as reference materials: Jadeite (Na), San Carlos olivine (Mg), disthene (Al), hypersthene (Si), sanidine (K), diopside (Ca), rutile (Ti), chromium oxide (Cr), rhodonite (Mn), and fayalite (Fe).

Trace element analyses were carried out using laser ablation-inductively coupled plasma mass spectrometry using an Analyte G2 Excimer laser ablation system (wavelength 193 nm) coupled to a Thermo Scientific Element 2 ICP-MS. The laser repetition rate was 10 Hz with a pulse energy of 3 J/cm^2. The ablated dry aerosol was transferred to the mass spectrometer by a He-Ar mixed gas flow, with volume fluxes of 0.8 and 0.85 l/min, respectively. ^{29}Si was selected as the internal standard applying SiO_2 contents determined by electron microprobe and the values given in the GeoReM database (Jochum et al. 2005) for the reference materials, respectively. USGS reference materials BCR-2G, BIR-1G and BHVO-2G were measured as unknown to monitor accuracy and precision. Data processing was carried out using the commercial

Table 1 Starting material

Sample	*P* (GPa)	*T* (°C)	SiO_2	TiO_2	Al_2O_3	Cr_2O_3	FeO	MgO	MnO	CaO	Na_2O	K_2O	Total
Starting material													
Metasome	–	–	41.96	2.73	10.04	b.d	11.02	18.54	0.16	12.71	1.55	0.76	99.57
Lherzolite	–	–	44.84	0.11	3.51	0.32	8.2	39.52	0.12	3.07	0.3	0.02	100.01
Strip heater glass													
KulX1-1500			41.9(2)	9.7(2)	9.4(1)	0.07(2)	9.7(2)	18.4(2)	0.16(2)	12.7(1)	1.59(3)	0.77(4)	97.4(5)

Major and minor element composition of starting material and the metasome glass produced with the strip heater are in wt.%. Uncertainties are given in parentheses

Table 2 Pyroxenes

Sample	*P* (GPa)	*T* (°C)		SiO_2	TiO_2	Al_2O_3	Cr_2O_3	FeO	MgO	MnO	CaO	Na_2O	K_2O	Total	Mg#
Clinopyroxene															
E169	1	1000	Lherzolite	45(1)	3.6(4)	8.8(7)	0.09(3)	5.3(3)	12.8(5)	0.10(3)	23.0(5)	0.53(6)	b.d	98.9(2)	81.5(8)
E169	1	1000	Metasome	47(2)	2(1)	8(1)	b.d	6.0(7)	12.3(9)	0.12(2)	22.6(3)	0.9(2)	b.d	99.1(4)	79(3)
E157	1	1100	Lherzolite	47.9(6)	1.7(2)	7.5(4)	0.2(2)	5.4(2)	13.6(8)	0.16(1)	22.5(6)	0.77(3)	b.d	99.7(2)	82(1)
E157	1	1100	Metasome	47(2)	2.4(9)	8(1)	0.14(8)	5.4(3)	12.8(6)	0.12(2)	22.6(3)	0.8(1)	b.d	99.0(5)	81(1)
E166	1	1150	Lherzolite	49(1)	1.5(3)	6.8(8)	0.65(3)	4.1(7)	15(1)	0.21(3)	21.4(6)	0.6(2)	0.07(7)	99.3(5)	87(3)
E166	1	1150	Metasome	47.5(8)	2.0(4)	7.7(7)	0.1(1)	5.3(3)	13.1(3)	0.11(2)	22.8(3)	0.8(1)	b.d	99.5(2)	81.9(9)
E158	1	1200	Lherzolite	50.1(4)	1.1(1)	7.0(4)	0.70(7)	2.4(2)	17.4(6)	0.34(5)	19.5(7)	0.67(8)	b.d	99.4(3)	93.0(4)
E149	3	1100	Lherzolite	51.7(2)	0.6(2)	6.0(5)	0.3(1)	4.2(2)	16.2(5)	0.39(0)	17.0(4)	2.2(1)	b.d	98.8(4)	87.5(5)
E149	3	1100	Metasome	49(1)	1.6(2)	7.3(8)	0.3(1)	5.7(4)	13.7(2)	0.16(4)	19.4(3)	1.5(4)	0.7(6)	98.3(2)	81(1)
E150[a]	3	1150	Lherzolite	52.5	0.7	6.4	0.3	3.9	16.9	0.39	16.9	1.9	b.d	99.8	88.8
E150	3	1150	Metasome	49(1)	1.9(5)	7.1(8)	0.09(2)	5.2(3)	14.1(6)	0.17(4)	21(1)	1.3(3)	b.d	99.2(5)	83(1)
E177	3	1200	Lherzolite	52(1)	1.1(3)	7(1)	0.3(1)	3.55(9)	17(1)	0.3(1)	19(1)	1.4(1)	b.d	100.1(1)	89.4(8)
E177	3	1200	Metasome	51.4(6)	1.4(2)	6.0(4)	0.13(3)	3.9(2)	16.0(5)	0.21(2)	19.1(4)	1.5(1)	b.d	99.7(5)	88.0(7)
E179	3	1250	Lherzolite	50.0(6)	1.4(3)	7.0(4)	0.48(3)	4.8(4)	17.3(1)	0.34(3)	15.7(4)	1.54(3)	b.d	98.9(2)	86.7(9)
E179	3	1250	Metasome	48.9(7)	1.9(2)	8.5(7)	0.12(6)	4.8(2)	14.5(5)	0.17(3)	19.2(7)	1.5(2)	b.d	99.6(4)	84.5(8)
E178	3	1300	Lherzolite	49.7(7)	1.5(1)	7.9(5)	0.2(1)	4.5(3)	15.5(8)	0.22(3)	18.3(4)	1.56(5)	b.d	99.4(3)	86(1)
E178	3	1300	Metasome	49.3(8)	1.7(2)	8.4(7)	0.15(3)	4.8(3)	14.9(5)	0.19(3)	18.5(3)	1.51(6)	b.d	99.5(3)	85(1)
E181	4	1100	Metasome	48(1)	1.8(3)	7.4(6)	0.1(1)	5.0(5)	13.2(5)	0.12(3)	22(1)	1.1(5)	b.d	98.8(4)	82(2)
E182	4	1200	Lherzolite	51(2)	1.6(5)	7(1)	0.28(7)	4.2(2)	16(1)	0.25(5)	18(1)	2.0(2)	b.d	98.9(2)	87(2)
E182	4	1200	Metasome	49(1)	2.0(2)	7.9(7)	0.1(1)	4.7(4)	13.9(7)	0.15(4)	20(1)	1.6(4)	b.d	98.8(3)	84(2)
E186	4	1250	Lherzolite	49.3(6)	1.3(1)	8.3(6)	0.14(4)	4.1(1)	15.5(4)	0.15(2)	18.4(3)	1.51(7)	b.d	98.7(3)	87.2(5)
E186	4	1250	Metasome	51.6(2)	0.7(1)	6.1(1)	0.36(5)	3.9(2)	17.9(6)	0.28(5)	16.1(8)	1.71(4)	b.d	98.8(3)	89.3(4)
E183	4	1300	Lherzolite	49.3(8)	1.6(3)	9(1)	0.13(5)	4.3(2)	15.1(8)	0.18(4)	18.1(4)	1.69(9)	b.d	99.0(3)	89.3(4)
E183	4	1300	Metasome	51.4(6)	0.9(2)	6.3(2)	0.39(3)	3.7(2)	17.3(5)	0.26(4)	16.8(7)	1.75(8)	b.d	98.9(3)	86(1)
E165	1	1100	Metasome	47(1)	2.0(4)	7.8(8)	0.2(2)	5.3(2)	12.9(5)	0.12(2)	22.9(2)	0.77(7)	b.d	99.3(2)	82(1)
E159	1	1200	Metasome	48(1)	1.6(5)	7(1)	0.12(7)	5.4(2)	13.3(3)	0.13(3)	22.9(1)	0.72(7)	b.d	99.5(4)	81.5(9)
Kula[a,b]	–	–	–	44.6	5.1	7.3	0.04	5.8	12.6	0.06	23.5	0.45	b.d	99.5	79
Kula[a,b]	–	–	–	40.1	1.8	7.1	0.28	4.6	14.2	0.09	22.5	0.68	0.05	99.7	85
Orthopyroxene															
E157	1	1100	Lherzolite	38.9(6)	b.d	3(1)	0.23(6)	8(1)	49(2)	0.51(4)	0.18(5)	0.07(5)	b.d	100.2(3)	92(1)

Major and minor element composition of clino- and orthopyroxene from experiments and Kula samples are in wt.%. Uncertainties are given in parentheses

[a]Single analysis. No error provided

[b]Mineral composition from the natural metasome starting material (Grützner et al. 2013)

Table 3 Other minerals

Sample	*P* (GPa)	*T* (°C)		SiO_2	TiO_2	Al_2O_3	Cr_2O_3	FeO	MgO	MnO	CaO	Na_2O	K_2O	Total	Mg#
Garnet															
E149	3	1100	Lherzolite	40.5(1)	0.6(1)	21.0(3)	0.87(7)	11.5(6)	17.0(3)	1.21(5)	6.5(2)	b.d	b.d	99.3(4)	70(1)
E150[a]	3	1150	Lherzolite	46.8	0.9	14.6	0.64	6	19.8	0.72	9.1	0.89	b.d	99.7	85.5
E150[a]	3	1150	Metasome	40.6	2.1	19.8	0.05	11.4	15	0.53	8.3	0.28	b.d	98.1	70.6
E177	3	1200	Lherzolite	42.2(2)	0.5(1)	20.3(9)	0.50	7.5(1)	23(1)	0.83(5)	5.2(2)	0.07(3)	b.d	99.7(5)	84.6(9)
E179[a]	3	1250	Metasome	41.5	1.1	21.9	0.34	8.1	19.6	0.6	7	0.09	b.d	100.2	81.6
E178[a]	3	1300	Lherzolite	41.4	1	22.5	0.50	7.7	19.6	0.59	6.8	0.06	b.d	100.2	82.8
E178	3	1300	Metasome	41.8(4)	0.8(1)	21.3(9)	0.34	7.6(2)	21.1(8)	0.60(1)	6.4(4)	b.d	b.d	100.2(2)	83.5(3)
E181[a]	4	1100	Metasome	40.1	1.2	21.6	0.062	10.4	15.3	0.51	9.5	0.22	b.d	98.9	72.8
E182[a]	4	1200	Lherzolite	40.7	1.2	22.6	0.22	8.3	19.3	0.76	6.5	0.11	b.d	99.7	80.9
E182	4	1200	Metasome	41.0(7)	1.4(1)	22.2(5)	0.10(4)	8.7(2)	17.4(5)	0.57(3)	7.8(3)	0.15(7)	b.d	99.4(4)	78.5(3)
E186	4	1250	Lherzolite	40.7(3)	1.3(2)	22.5(4)	0.19(2)	6.7(2)	19.7(3)	0.48(3)	7.6(3)	0.09(3)	b.d	99.4(5)	84.1(6)
E186	4	1250	Metasome	41.7(3)	0.62(4)	22.2(8)	0.8(1)	6.0(4)	21.2(4)	0.72(5)	6.2(6)	0.09(6)	b.d	99.4(4)	86.5(8)
E183	4	1300	Lherzolite	40.7(2)	1.33(9)	22.5(1)	0.18(8)	7.5(2)	18.7(3)	0.49(3)	7.9(2)	0.07(3)	b.d	99.7(3)	81.9(6)
Amphibole															
E169[a]	1	1000	Metasome	39.3	5.1	13.9	b.d	8.1	13.4	0.08	12.3	2.3	1.7	96.3	75.1
E157	1	1100	Metasome	39.9(4)	4.6(4)	13.8(2)	b.d	8.1(4)	13.8(2)	0.11(1)	12.1(1)	2.3(1)	1.66(3)	96.4(3)	75.5(9)
E149	3	1100	Metasome	40.1(8)	4.7(4)	13.5(6)	b.d	8.0(6)	13.8(2)	0.10(1)	12.6(9)	2.1(2)	1.6(2)	96.5(3)	75(1)
E150	3	1150	Metasome	40.7(6)	4.1(5)	14.0(1)	0.04(3)	7.0(9)	14.8(9)	0.10(3)	11.1(5)	2.48(9)	2.2(3)	96.5(2)	79(3)
E181[a]	4	1100	Metasome	39	5.0	14.6	0.08	8.2	13.5	0.07	12.1	2.4	1.7	96.7	75.1
Kula[a,b]	–	–	–	39.9	4.4	14.5	0.04	8.8	13.6	0.13	12.0	2.5	1.6	97.7	73
Kula[a,b]	–	–	–	40.1	4.2	14.0	0.41	8.3	14.2	0.11	12.0	2.5	1.7	97.7	75
Phlogopite															
E150	3	1150	Metasome	37.7(5)	4.1(2)	15.7(2)	0.07(3)	3.7(1)	22.1(2)	0.07(2)	0.2(1)	0.80(6)	9.3(1)	93.7(6)	75.3(6)
E177	3	1200	Metasome	37.7(5)	4.1(2)	15.7(2)	0.08(2)	3.7(1)	22.1(2)	0.06(2)	0.12(4)	0.80(6)	9.3(1)	93.7(7)	82.0(5)
E181	4	1100	Metasome	38.2(3)	2.54(7)	15.4(5)	b.d	4.9(1)	22.2(2)	0.06(1)	0.2(1)	0.63(3)	9.5(1)	93.7(3)	89.1(2)
E182	4	1200	Metasome	37.4(8)	4.50(9)	15.4(2)	b.d	4.66(4)	20.6(4)	0.08(1)	0.15(5)	0.35(2)	9.8(1)	93(1)	88.9(2)
Rhönite															
E169[a]	1	1000	Metasome	26(1)	9(1)	16.6(9)	0.08(3)	16.2(6)	14.9(9)	0.11(2)	11.9(3)	1.2(2)	0.02(2)	96(2)	
E157	1	1100	Metasome	26.1(2)	10.9(2)	17.1(1)	0.07(1)	14.7(3)	15.3(1)	0.11(2)	12.31(2)	1.16(5)	0.04(2)	97.8(3)	
Kula[a,b]	–	–	–	25.0(2)	10.8(2)	18.4(1)	0.2(1)	17.3(3)	14.3(3)	0.12(2)	12.2(2)	1.13(6)	0.05(4)	99.5(3)	

Major and minor element composition of garnet, amphibole, phlogopite, and rhönite from experiments and Kula samples are in wt.%. Uncertainties are given in parentheses. b.d. = below detection limit

[a] Single analysis. No error provided

[b] Mineral composition from the natural metasome starting material (Grützner et al. 2013)

Table 4 Experimental run conditions

Sample	*P* (GPa)	*T* (°C)	Run duration (h)	Phase assemblage	
				Lherzolite	Metasome
Metasome+Lherzolite (volume 1:1)					
E169	1	1000	42	ol, cpx, plg, opx, calc	ab, cpx, ol, rho, sp, il, krs
E157	1	1100	157	ol, cpx, opx, sp	cpx, ol, krs, rho, glass
E166	1	1150	24	ol, cpx, glass	cpx, ol, glass
E158	1	1200	20	ol, cpx, glass	glass
E149	3	1100	24	ol, cpx, grt	cpx, ol, krs, Cr-sp, Mg-il
E150	3	1150	20	ol, cpx, grt, glass	cpx, ol, grt, krs, phl, Mg-il, glass
E177	3	1200	24	ol, cpx, grt*, glass	cpx, ol, grt, phl, glass
E179	3	1250	20	ol, cpx, grt, glass	cpx, ol, grt, glass
E178	3	1300	20	ol, cpx, grt, glass	cpx, ol, grt, glass
E181	4	1100	20	ol, cpx, grt	cpx, ol, grt, phl, krs
E182	4	1200	23	ol, cpx, grt, glass	cpx, ol, grt, phl, glass
E186	4	1250	20	ol, cpx, grt, glass	cpx, ol, grt, glass
E183	4	1300	20	ol, cpx, grt, glass	cpx, ol, grt, glass
Only metasome					
E165	1	1100	24	–	cpx, ol, glass
E159	1	1200	22	–	cpx, ol, glass

Table 5 Glass compositions

Sample	*P* (GPa)	*T* (°C)	SiO_2	TiO_2	Al_2O_3	Cr_2O_3	FeO	MgO	MnO	CaO	Na_2O	K_2O	Total
Metasome melt													
E165	1	1100	40.3(2)	4.5(1)	16.6(4)	b.d	9.9(3)	4.9(4)	0.23(2)	10.9(5)	3.5(2)	1.85(9)	92.7(4)
E159	1	1200	40.9(3)	3.6(4)	14.3(2)	b.d	8.0(3)	9.2(1)	0.17(2)	13.8(3)	3.1(1)	1.28(5)	94.5(6)
Reaction melt													
E157	1	1100	49.0(5)	1.5(2)	18(1)	b.d	5.0(7)	5.9(5)	0.14(2)	5.8(9)	4.9(5)	3.8(3)	95(1)
E166	1	1150	41(2)	4.2(2)	14(2)	b.d	7.7(6)	7.2(2)	0.28(4)	13.8(7)	2.4(2)	1.20(8)	92(4)
E158b	1	1200	42.5(2)	2.5(1)	15.23(9)	0.06(1)	5.53(9)	10.54(6)	0.25(2)	13.0(2)	3.05(6)	0.72(4)	93.3(3)
E158a	1	1200	44.9(2)	2.3(1)	16.4(3)	b.d	4.1(3)	9.3(1)	0.33(2)	11.6(1)	3.7(1)	1.07(4)	93.8(4)
E150	3	1150	32.8(4)	7.0(2)	8.9(1)	b.d	9.3(2)	11.1(4)	0.41(3)	10.8(3)	2.2(4)	1.5(2)	84.0(6)
E177	3	1200	33.5(8)	6.1(4)	9.8(4)	b.d	6.8(3)	10.9(8)	0.38(3)	10.1(8)	4.9(8)	1.3(3)	83(1)
E179	3	1250	38.2(2)	5.4(2)	11.0(1)	0.06(2)	8.5(1)	12.00(6)	0.378(3)	8.9(1)	3.00(6)	1.32(5)	90.0(4)
E178	3	1300	38.0(4)	5.6(3)	11.1(5)	b.d	8.5(4)	11.3(1)	0.36(3)	9.4(7)	2.9(1)	1.3(1)	90.0(9)
E182	4	1200	29(1)	7.3(8)	7.6(5)	b.d	8.8(6)	12.5(3)	0.34(5)	12(2)	2.5(3)	3.1(5)	83(2)
E186	4	1250	36.1(2)	5.7(1)	8.78(6)	b.d	8.8(1)	14.31(6)	0.36(3)	9.8(1)	2.77(6)	2.39(5)	89.1(3)
E183	4	1300	35.9(2)	6.2(2)	9.6(1)	b.d	8.3(1)	12.6(1)	0.36(2)	9.4(4)	3.1(1)	2.39(8)	88.4(5)

Major and minor element composition of experimental glasses are in wt.%. Uncertainties are given in parentheses. b.d. = below detection limit

software GLITTER 4.4.1 (Griffin et al. 2008) where possible, laser spots were chosen at the same locality as the microprobe spots. Typical spot sizes were 20 or 35 µm. Trace element data are listed in Table 6.

Results

Petrography of experimental run products

We conducted 15 experiments at 1000–1300 °C and 1, 3 and 4 GPa. At 1 GPa we ran two types of experiments: (1) In the *only-metasome experiments*, the capsule was

Table 6 Trace element composition of experimental glasses

Element	Strip heater glass	1 GPa		3 GPa				4 GPa			1 GPa (only metasome)
	KulX1-1500	E166	E158	E150	E177	E179	E178	E182[a]	E186	E183	E159
Cs	0.075(9)	b.d	0.6(3)	1.6(3)	1.7(4)	1.5(2)	1.5(2)	1.0	1.08(8)	1.3(1)	0.13(1)
Rb	9.75(9)	14(1)	11(2)	16(2)	15(2)	31(3)	39.2(6)	17.1	34.7(9)	41.6(9)	14.7(3)
Ba	322(3)	452(25)	329(28)	880(23)	907(130)	897(92)	1065(14)	699	928(22)	1140(17)	419(10)
Th	0.65(2)	1.07(8)	1.0(3)	5.0(6)	8(1)	3.0(3)	2.9(1)	2.3	2.39(8)	2.88(5)	0.79(3)
U	0.170(4)	0.32(5)	0,5(2)	2.2(2)	3.5(6)	1.3(1)	1.17(2)	0.9	0.95(5)	1.14(4)	0.23(2)
Nb	38.9(5)	56(3)	34(3)	184(7)	267(35)	123(11)	127(3)	134	108(3)	132(1)	47(2)
Ta	2.41(4)	3.2(2)	2.0(3)	10.1(6)	15(2)	7.2(8)	7.6(2)	7.2	6.5(3)	7.9(1)	2.7(1)
La	12.5(1)	20(1)	15(2)	79(5)	112(18)	62.(6)	60(1)	50.8	44(1)	55.9(9)	15.5(4)
Ce	32.4(3)	46(2)	31(2)	148(11)	195(33)	89(9)	92(1)	81.7	84(2)	97(1)	40(1)
Pb	0.24(4)	b.d	b.d	1.3(5)	0.18(8)	b.d	b.d	0.13	0.07(1)	0.06(1)	b.d
Pr	4.75(7)	6.5(3)	4.6(3)	19(1)	25(4)	12(1)	12.7(3)	10.5	11.6(4)	13.2(2)	5.6(2)
Sr	430(4)	601(40)	439(40)	1707(87)	2238(354)	1144(101)	1162(14)	962	1049(25)	1163(18)	565(13)
Nd	22.7(3)	30(1)	20(2)	84(7)	98(16)	52(4)	54(1)	44.6	51(2)	57(1)	27.0(8)
Sm	5.7(1)	7.0(7)	5.0(3)	16(1)	17(4)	10(2)	10.5(3)	8.8	10.7(8)	11.5(8)	6.7(3)
Zr	100.3(5)	133(7)	116(7)	334(11)	371(46)	234(22)	246(5)	195	231(6)	258(5)	143(3)
Hf	3.29(8)	4.4(4)	6(1)	16.0(7)	16(2)	11(1)	11.0(4)	8.4	10.7(4)	11.5(4)	4.3(2)
Eu	1.84(4)	2.6(2)	1.5(1)	5.1(4)	4.4(7)	2.9(4)	3.1(1)	2.1	3.2(2)	3.4(2)	2.2(1)
Gd	5.5(1)	6.3(2)	4.5(2)	11(1)	12(3)	7.4(7)	8.1(3)	5.7	8.2(5)	8.8(3)	6.0(3)
Tb	0.78(1)	0.99(7)	0.63(4)	1.28(9)	1.3(2)	0.90(9)	1.00(4)	0.62	1.02(5)	1.01(6)	0.85(3)
Dy	4.45(7)	5.6(3)	3.7(3)	6.2(5)	6(1)	4.2(5)	4.7(3)	2.7	4.9(3)	4.9(2)	4.8(2)
Y	20.5(1)	26(1)	19(2)	25(1)	24(4)	19(2)	21.5(5)	10.4	20.3(7)	19.9(5)	22.6(6)
Ho	0.82(1)	1.07(8)	0.70(5)	0.9(1)	0.8(2)	0.77(8)	0.76(7)	0.48	0.82(6)	0.79(6)	0.94(4)
Er	2.07(4)	2.4(3)	1.8(2)	1.8(2)	1.9(5)	1.5(3)	1.7(1)	0.85	1.7(1)	1.7(2)	2.3(2)
Tm	0.26(1)	0.35(3)	0.21(2)	0.19(3)	0.18(4)	0.15(3)	0.19(3)	0.12	0.19(3)	0.17(2)	0.28(1)
Yb	1.61(3)	2.2(2)	1.4(1)	1.1(1)	0.8(4)	0.9(2)	1.00(9)	0.57	1.0(1)	1.0(2)	1.8(1)
Lu	0.225(7)	0.42(2)	0.19(1)	0.12(1)	0.12(3)	0.16(2)	0.14(1)	0.05	0.13(1)	0.12(1)	0.25(2)

Values are in µg/g. Uncertainties are given in parentheses. b.d. = below detection limit

[a]Based on two analyses. No error provided

loaded with the starting material comprised of natural metasome. Only two experiments were made at 1 GPa and 1100, 1200 °C. (2) Most experiments of this study are *reaction-experiments*. For each of this type of experiment, a layer of metasome was placed in the bottom of the noble metal capsule and a layer of lherzolite was placed above the metasome. At 3 and 4 GPa, all conducted experiments were reaction-experiments.

The experimental capsules were geochemically and mineralogically thoroughly characterized and the cross-sections of all experimental runs (Figure S5) as well as a comprehensive dataset consisting of individual mineral and glass analyses (EPMA and LA-ICP-MS raw data files) can be found in the supplementary dataset of the electronic appendix. Cation calculations for the different mineral phases were done with the MinPlot software from Walters (2022).

After melting, the two different residual lithologies in the experiments (lherzolite and amphibole-clinopyroxene-rich metasome) are generally wehrlitic, and even at higher melt fractions, residues of both metasome and lherzolite remain in the capsule. They can be distinguished from each other by the relative olivine and clinopyroxene abundance: the lherzolite residue is olivine dominated and appears darker on backscattered electron images (BSE); the metasome and its residue are dominated by clinopyroxene (at 3–4 GPa), which appears brighter on BSE images (Figs. 1, 2, 3). Thus, incongruent melting of amphibole in the metasome produced wehrlitic residue and the melt then reacted with orthopyroxene from the lherzolite, which again produced wehrlitic residue with the different olivine: clinopyroxene ratios. In other words, the mixing of the incongruent and reaction melts within the metasome + lherzolite lithology should be capable of explaining the composition of various alkaline melts produced in the course of our experiments.

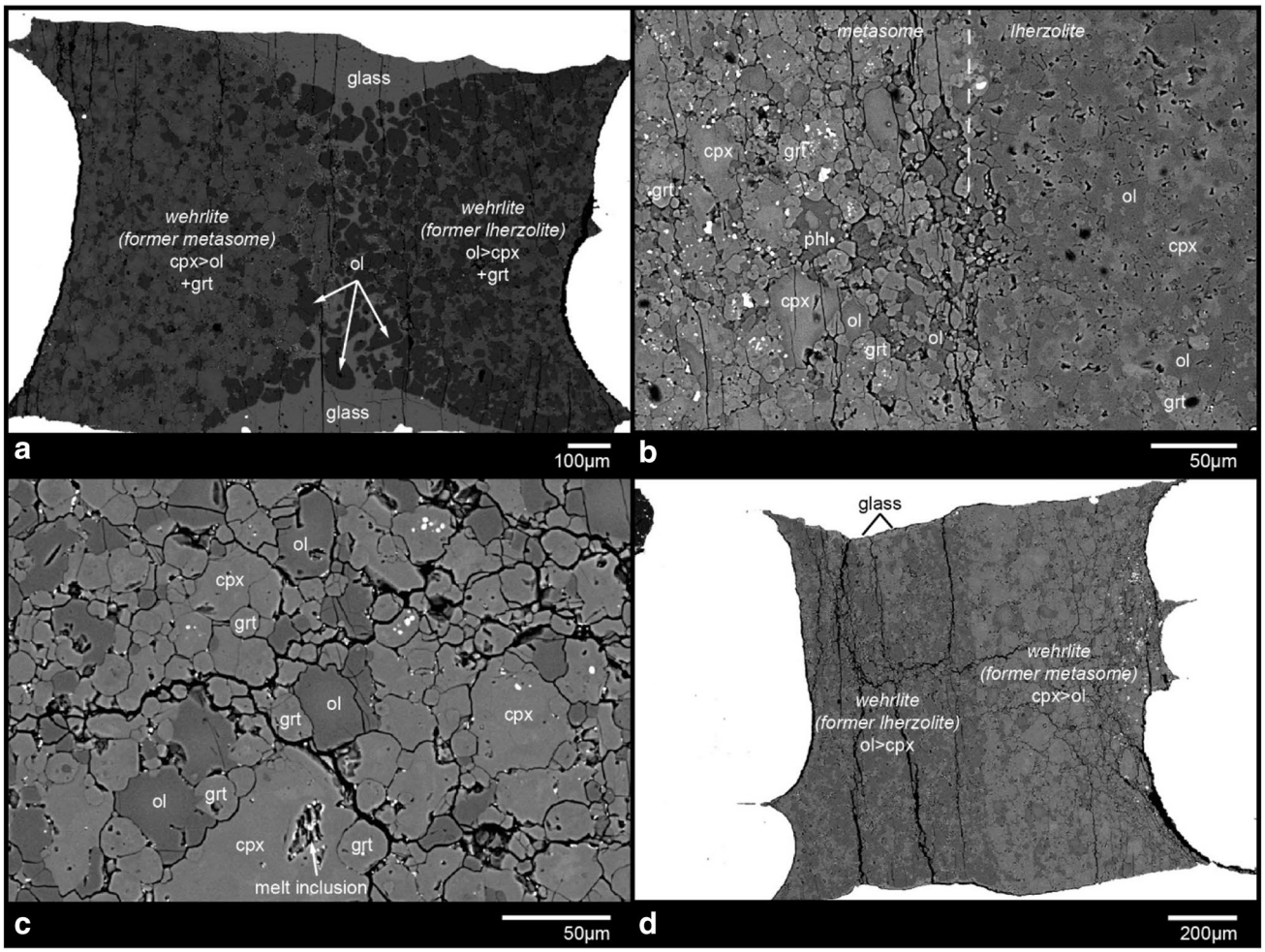

Fig. 1 SEM images of experiments at 4 GPa. **a** E186 (1250 °C): Wehrlitic residues of former metasome and lherzolite can be distinguished by the different olivine and clinopyroxene content. The metasome residue is richer in clinopyroxene while the lherzolite residue is richer in olivine. **b** E181 (1100 °C): At 4 GPa subsolidus phlogopite is the dominant volatile bearing phase. **c** E182 (1200 °C): At 4 GPa no melt pockets remain between the grains of the residue. The mobile melts migrate to the capsule walls. **d** E182 (1200 °C): As in (**a**) the wehrlites of both lithologies have different olivine and clinopyroxene content. The first melts at 4 GPa can be found close to the capsule walls. Mineral abbreviations are *cpx* clinopyroxene, *grt* garnet, *ol* olivine

In all subsolidus experiments and runs with low melt fraction, the metasome phase is well crystallized. In contrast, the synthetic lherzolite shows very poor crystallization at low temperatures and subsolidus conditions. As temperatures increase and the lherzolite reacts with the melt, the remaining minerals show good crystallization, too (Fig. 1b).

1 GPa reaction experiments

In the reaction experiment at 1 GPa and near-solidus conditions (~ 1100 °C), the first melting is observed in the metasome (Fig. 2). The melt pockets remain attached to the residual grains and show no reaction with the peridotite that remains still poorly crystallized. With higher degrees of melting (at 1150 °C), amphibole vanishes and only olivine and clinopyroxene remain in the metasome. As the melt volume increases further, it creates a layer between lherzolite and metasome (Fig. 2c). At 1200 °C the interface between the metasome and lherzolite disappears, that is, the capsule contains glass that coexists with a crystal mush of olivine and clinopyroxene (Fig. 2d).

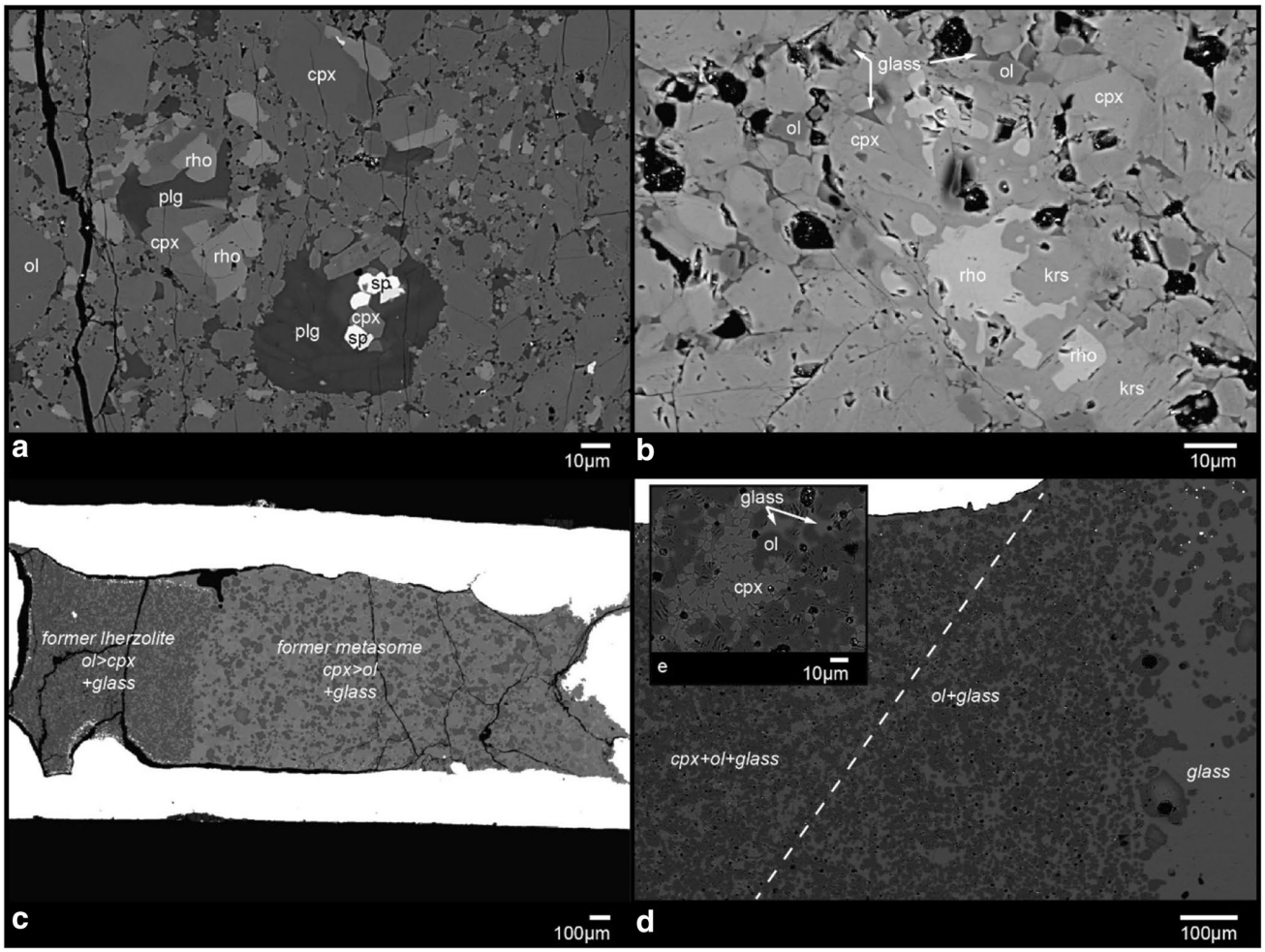

Fig. 2 SEM images of experiments at 1 GPa. **a** E169 (1000 °C): The amphibole is not stable at these conditions in the experimental system. Instead, its breakdown products including plagioclase, rhönite, and spinel can be found. **b** E157 (1100 °C): First melt at 1 GPa can be found in melt pockets together with clinopyroxene, kaersutite, olivine, and rhönite. **c** E158 (1150 °C): At 1 GPa the residue is wehrlitic to (clino)pyroxenitic with abundant glass. **d** and **e** E158 (1200 °C): At 1200 °C the interface between the metasome and lherzolite disappears, that is, the capsule contains glass, which coexists with a crystal mush of olivine and clinopyroxene. Mineral abbreviations are *cpx* clinopyroxene, *grt* garnet, *krs* kaersutite, *ol* olivine, *plg* plagioclase, *rho* rhönite, *sp* spinel

1 GPa only-metasome experiments

Two *only-metasome* melting experiments at 1 GPa were conducted as test-runs to check for differences in the reaction experiments. The differences are small but visible: at 1150 °C, amphibole is molten, and the melt does not separate from the residue but remains within the metasome. At 1200 °C, the melt volume strongly increased and the melt was able to escape the metasome and it concentrates at the top of the capsule coexisting also with olivine and clinopyroxene of the same composition as in the reaction experiments. It occurs that in the *only-metasome* runs the solidus is slightly lower than in the reaction experiments. Also, no other minor phases like rhönite were observed at 1150 °C in these experiments.

3 GPa experiments

At 3 GPa no melt pockets can be found at the earliest melting stage. The first detected melt (1150 °C) appears directly at the capsule wall. As the melt volume increases, a layer of melt + olivine forms at the former contact of lherzolite and metasome (Fig. 3). This layer remains stable, also at the highest temperature that was set up for this

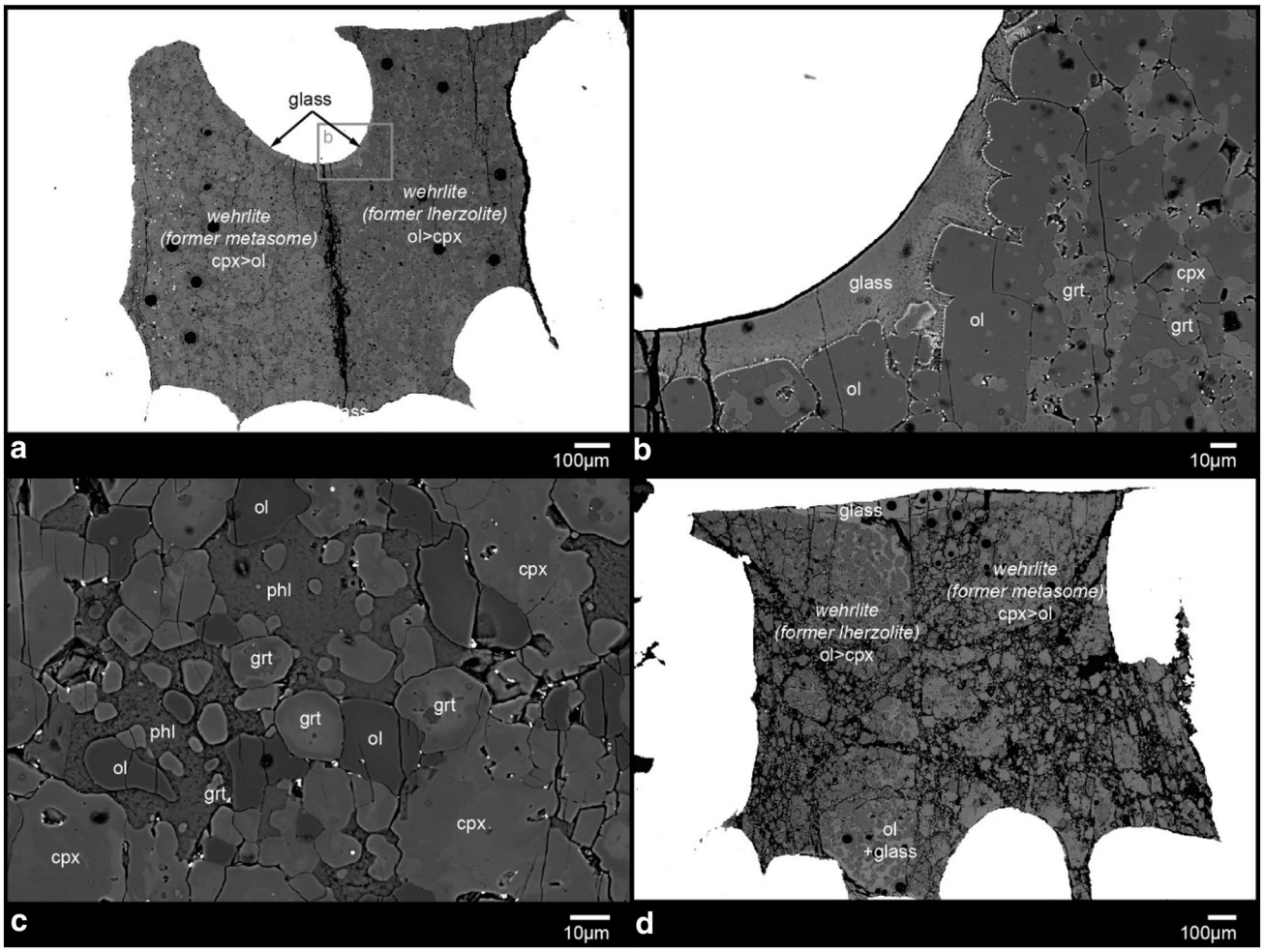

Fig. 3 SEM images of experiments at 3 GPa. **a**, **b** E177 (1200 °C): The metasome residue is richer in clinopyroxene while the lherzolite residue is richer in olivine. First melting is trapped at the capsule wall. **c** E155 (1150 °C): Phlogopite is stable up to 1200 °C. **d** E178 (1300 °C): with increasing melt fraction the melt plus olivine form a layer between the two residue lithologies. Mineral abbreviations are *cpx* clinopyroxene, *grt* garnet, *ol* olivine, *phl* phlogopite

study (1300 °C). In contrast to 1 GPa experiments, garnet is stable at subsolidus conditions. It remains in the residue at higher temperatures in coexistence with the melt and forms wehrlite together with olivine and clinopyroxene from both the metasome and the lherzolite. Garnet can show relatively complex textures: many grains contain olivine and pyroxene inclusions showing slight zoning from core to rim (Fig. 3c). This is not only the case for garnet in subsolidus experiments, but also in the presence of melt and demonstrates that garnet does not equilibrate as fast as pyroxene during the experiments.

4 GPa experiments

At 4 GPa, the first melting can be observed at 1200 °C (E182). The melt accumulates at the capsule wall, which is typically the hottest region within the capsule in this experimental setup. Ideally, the residue of metasome and peridotite forms together an hourglass shape (Fig. 1a). Larger melt volumes form a layer of melt+olivine at 1250 and 1300 °C. No intergranular melt pockets were found but a few melt inclusions remained entrapped within single crystals of clinopyroxene in the former metasome phase (Fig. 1c). Similar to the 3 GPa experiments, the residue is wehrlitic.

Mineral compositions

Olivine and clinopyroxene are present in the lherzolite and metasome of all experimental runs in this study, whereas orthopyroxene was only found at 1 GPa and 1100 °C (Table 2). The coexisting alumina-bearing phases are Fe-Cr-spinel+plagioclase subsolidus at 1 GPa, garnet+spinel subsolidus at 3 GPa and garnet at 4 GPa. Spinel and plagioclase

disappear at temperatures ≥ 1100 °C (1 GPa). Garnet is stable in all runs at 3 and 4 GPa up to the highest experimental temperature of 1300 °C.

Olivine

The overall Mg# (Mg/(Mg + Fe)*100) of experimental olivines ranges from 79.5 to 94.2. Subsolidus lherzolite olivines have a Mg# of 88 ± 2 at 3 GPa and 88.3 ± 0.8 at 4 GPa. At 1 GPa olivine in the lherzolite is lower with 80.4 ± 8. The Mg# in the subsolidus metasome ranges from 80.7 ± 0.5 at 1 GPa to 82.2 ± 1.7 at 3 GPa and 82.4 ± 0.8 at 4 GPa. This is in good agreement with a metasome olivine Mg# of 80 ± 1, measured in the natural host material (Grützner et al. 2013). The general trend for all pressures shows increasing Mg# with increasing temperature and melt fraction. At 3 and 4 GPa, above 1250 °C, metasome and lherzolite olivines cannot be distinguished by their Mg# anymore. Their values overlap and range from 89.3 to 91.7. At 1 GPa olivines from lherzolite and metasome do not fully align at high temperatures and high melt fractions. E158, at 1200 °C and 1 GPa, is the only experiment that bears olivine with Mg# above 91.7: large olivines float within the melt and show Mg# between 91.6 and 94.2. In the coexisting crystal mush, olivines have a Mg# of 87 ± 1.5.

Other oxides like Al_2O_3 (0.13 ± 0.07), CaO (0.24 ± 0.08), and MnO (0.35 ± 0.03) show no clear difference between lherzolite and metasome olivines, or trends with increasing pressure, temperature and melt fraction. Olivine compositions are listed in Table 7. Mg# distribution in olivines is shown in Figure S1.

Table 7 Olivines

Sample	*P* (GPa)	*T* (°C)		SiO_2	TiO_2	Al_2O_3	Cr_2O_3	FeO	MgO	MnO	CaO	Na_2O	K_2O	Total	Mg#
E169	1	1000	Lherzolite	38.3(2)	b.d	b.d	b.d	18.3(6)	41.4(5)	0.38(3)	0.25(9)	b.d	b.d	98.6(2)	80.4(8)
E169	1	1000	Metasome	38.3(1)	b.d	b.d	b.d	18.1(5)	41.7(3)	0.37(2)	0.14(8)	b.d	b.d	98.7(3)	80.7(5)
E157[a]	1	1100	Lherzolite	38.9	b.d	0.75(3)	0.12	14.7	44.2	0.64	0.2(1)	b.d	b.d	99.5	84.6
E157	1	1100	Metasome	38.5(3)	b.d	b.d	b.d	17(2)	42(2)	0.36(3)	0.15(5)	b.d	b.d	98.9(4)	81(2)
E166	1	1150	Lherzolite	39.9(2)	b.d	0.12(9)	0.07(3)	9.1(1)	49.0(3)	0.40(2)	0.40(7)	b.d	b.d	99.1(4)	90.7(2)
E166	1	1150	Metasome	39.5(4)	b.d	0.04(1)	b.d	13(2)	46(1)	0.32(4)	0.25(9)	b.d	b.d	99.3(4)	86(2)
E158	1	1200	Lherzolite	40.5(3)	b.d	0.17(8)	b.d	7.0(7)	51.1(7)	0.37(8)	0.34(6)	b.d	b.d	99.5(4)	93.2(7)
E158	1	1200	Metasome	39.2(3)	b.d	0.09(6)	b.d	13(1)	46(1)	0.27(2)	0.26(8)	b.d	b.d	98.8(2)	87(2)
E149	3	1100	Lherzolite	39.0(4)	b.d	0.2(1)	b.d	12(2)	47(2)	0.41(3)	0.16(7)	b.d	b.d	98.7(4)	88(2)
E149	3	1100	Metasome	38.4(1)	b.d	0.09(5)	b.d	17(1)	43(1)	0.34(3)	0.19(6)	b.d	b.d	99.3(4)	82(2)
E150	3	1150	Lherzolite	40.1(3)	b.d	0.08(3)	b.d	10.6(7)	48.2(5)	0.43(4)	0.18(8)	b.d	b.d	99.7(4)	89.2(7)
E150	3	1150	Metasome	39.4(3)	b.d	0.10(4)	b.d	15(1)	44(1)	0.33(3)	0.19(6)	b.d	b.d	99.3(4)	84(2)
E177	3	1200	Lherzolite	40.1(3)	b.d	0.2(1)	b.d	10.1(5)	48.8(6)	0.37(3)	0.15(4)	b.d	b.d	99.8(3)	89.7(6)
E177	3	1200	Metasome	39.5(3)	b.d	0.12(6)	b.d	13(2)	46(1)	0.36(4)	0.16(2)	b.d	b.d	99.2(4)	86(2)
E179	3	1250	Lherzolite	40.2(1)	b.d	0.08(2)	b.d	10.0(2)	48.8(4)	0.35(2)	0.16(2)	b.d	b.d	99.8(5)	89.8(2)
E179	3	1250	Metasome	40.4(1)	b.d	0.09(1)	b.d	10.2(2)	48.5(6)	0.33(2)	0.19(2)	b.d	b.d	99.7(6)	89.6(2)
E178	3	1300	Lherzolite	40.2(3)	b.d	0.08(2)	b.d	10.0(3)	48.8(4)	0.33(2)	0.18(3)	b.d	b.d	99.8(5)	89.8(2)
E178	3	1300	Metasome	40.5(1)	b.d	0.10(3)	b.d	9.8(1)	48.7(3)	0.31(2)	0.24(3)	b.d	b.d	99.7(4)	90.0(1)
E181	4	1100	Lherzolite	39.4(2)	b.d	0.04(1)	b.d	11.5(7)	47.7(7)	0.34(4)	0.11(2)	b.d	b.d	99.2(3)	88.3(8)
E181	4	1100	Metasome	38.3(2)	b.d	0.05(1)	b.d	16.7(7)	43.0(7)	0.36(3)	0.13(4)	b.d	b.d	98.6(3)	82.4(8)
E182	4	1200	Lherzolite	39.5(3)	b.d	0.1(1)	b.d	10.7(4)	48.1(4)	0.32(4)	0.18(5)	b.d	b.d	99.0(4)	89.1(4)
E182	4	1200	Metasome	39.2(4)	b.d	0.04(1)	b.d	13(1)	46(1)	0.34(2)	0.17(2)	b.d	b.d	99.0(2)	87(2)
E186	4	1250	Lherzolite	39.7(2)	b.d	0.10(2)	b.d	8.6(1)	49.9(2)	0.27(3)	0.24(2)	b.d	b.d	98.9(3)	91.4(1)
E186	4	1250	Metasome	39.8(2)	b.d	0.15(9)	b.d	8.6(1)	49.7(2)	0.28(2)	0.22(3)	b.d	b.d	98.9(3)	91.3(1)
E183	4	1300	Lherzolite	39.8(3)	b.d	0.08(3)	b.d	9.8(8)	48.9(8)	0.29(2)	0.23(3)	b.d	b.d	99.2(3)	90.0(9)
E183	4	1300	Metasome	39.9(3)	b.d	0.08(2)	b.d	9.0(1)	49.7(2)	0.28(2)	0.20(3)	b.d	b.d	99.2(4)	91.0(1)
E165	1	1100	Metasome	38.9(2)	b.d	0.05(1)	b.d	15.3(4)	44.0(6)	0.30(2)	0.29(8)	b.d	b.d	99.0(3)	84.1(6)
E159	1	1200	Metasome	39.3(2)	b.d	0.05(3)	b.d	14(2)	45(1)	0.29(4)	0.3(1)	b.d	b.d	99.1(4)	86(2)

Uncertainties are given in parentheses. b.d. = below detection limit. Major and minor element composition of olivine are in wt.%

[a]Single analysis. No error provided

Clinopyroxene

Clino- and orthopyroxene compositions are listed in Table 2. Mg# distribution and Ca/Al_2O_3 ratios in clinopyroxenes are shown in Figure S2 and Figure S3, respectively.

Clinopyroxene Mg# ranges from 71.7 to 93.9. In lherzolite at 1 GPa, the Mg# increases from 82 ± 1 to 93.0 ± 0.4 with increasing temperature and melt fraction. However, at 3 and 4 GPa, the Mg# remains relatively constant, ranging from 87.5 ± 0.5 to 86 ± 1 at 3 GPa and from 87 ± 1 to 89.3 ± 0.4 at 4 GPa.

In the metasome, subsolidus clinopyroxene has a lower Mg# of 79 ± 3 at 1 GPa, 81 ± 1 at 3 GPa and 82 ± 2 at 4 GPa. This is close to the average metasome clinopyroxene Mg# of 81 ± 2, measured in the natural starting material (Grützner et al. 2013). While at 1 GPa and 1200 °C only one type of clinopyroxene was found in the crystal mush, at 3 and 4 GPa clinopyroxenes from former metasome and former lherzolite can still be distinguished at 1300 °C experiments: Mg# at 3 and 4 GPa in the former metasome are 85 ± 1 and 86 ± 1, respectively.

The difference in clinopyroxene Mg# between metasome and lherzolite is also pressure-related: clinopyroxene at 1 GPa has Mg# between 77 and 84.5, while at 3 and 4 GPa, the Mg# ranges from 83 to 90.5. This is consistent with the CaO content of the analyzed grains, which ranges from about 20.9–23.4 wt.% for the low Mg# group and from about 9.7–18.7 wt.% for the high Mg# group. Moreover, low temperature metasome clinopyroxene at 3 and 4 GPa shows a wide variety in Mg# and CaO content, spanning the entire range of both groups with Mg# ranging from 79.5 to 87.2 and CaO from 17.4 to 23.3 wt.%. At 1 GPa and 1200 °C, clinopyroxene has the highest Mg# (91.7–93.8) but a medium CaO content of 17.8–20.7 wt.%. Additionally, there is a general correlation between increasing Mg# and an increasing amount of MnO and Cr_2O_3, as well as decreasing TiO_2 concentrations. Subsolidus clinopyroxene at 1 GPa has the highest TiO_2 (3.2 ± 8 wt.%) concentrations, and clinopyroxene from crystal mush at 1 GPa and 1300 °C has the highest Cr_2O_3 (0.7 ± 0.07 wt.%) concentration.

Clinopyroxene Cr# (Cr/(Cr + Al)*100) ranges from 0 to 18.5 (Figure S4). The restitic lherzolite at 1 GPa and high melt fraction (1150–1200 °C) has the highest values. At 1 GPa, Cr# increases significantly in the lherzolite component with rising temperature/melt fraction (1.7 ± 0.7 to 11.6 ± 1.1) and slightly in the metasome component (0.8 ± 0.5 to 2.3 ± 1.4). At 3 GPa, no clear trend can be observed for the metasome or the lherzolite. At 4 GPa, the Cr# of the metasome clinopyroxenes increases substantially (2.0 ± 1.4 to 7.6 ± 0.5) with increasing temperature/melt fraction, while the Cr# in lherzolite clinopyroxenes slightly decreases (4.7 ± 1.6 to 2.1 ± 0.8).

Garnet

Garnet is stable at 3 and 4 GPa at all experimental temperatures from 1100 to 1300 °C. Element concentration and Mg# trends are less obvious than for olivine or clinopyroxene. Mg# spread from 70.6 to 88.6. Low Mg#s in garnet were found in the subsolidus runs at 3 GPa (70 ± 1) and 4 GPa (72.8), as well as in the metasome phase of the 3 GPa run at 1150 °C (70.6) with a small melt fraction. With increasing temperature and melt fraction, all measured garnets have Mg# > 80.

The overall CaO content ranges from 4.8 to 11.4 wt.%, TiO_2 from 0.3 to 2.1 wt.% and Cr_2O_3 up to 1.7 wt.%. TiO_2 and Cr_2O_3 concentrations show opposing behavior but no temperature- or pressure-dependent trend. Moreover, both the highest and the lowest concentrations of these oxides were analyzed in garnets of the same sample (E186): At 4 GPa and 1250 °C lherzolite garnet has a low Cr_2O_3 content of 0.20(2) wt.% and TiO_2 ranging from 0.8 to 1.9 wt.%; metasome garnet has a low TiO_2 concentration of 0.57(8) wt.% and Cr_2O_3 ranges from 0.5 to 1.7 wt.% (Table 3).

Amphibole and phlogopite

Amphibole is stable at 1 GPa and 1100 °C, coexisting with low melt fractions and rhönite (Fig. 2). At 3 GPa, it is present from the subsolidus experiment at 1100 °C up to the low melt fraction run at 1150 °C. Phlogopite was not found in the subsolidus run at 3 GPa. It coexists with amphibole at 1150 °C and remains stable even at 1200 °C, even when amphibole has already melted (Fig. 3). At 4 GPa, two amphibole grains were analyzed, but phlogopite is the dominant volatile-bearing phase. Amphibole disappears with the first melt at 1200 °C, while phlogopite remains stable (Fig. 1). However, no phlogopite was found at 1250 °C.

The amphibole grains at 4 GPa do not show any significant compositional differences compared to amphiboles at lower pressures, which could explain their stability at such high pressure. We explain that despite using a fine-grained powder as starting material, the larger amphibole grains likely survived the crushing process and remained metastable during the subsolidus experiment.

The composition of the amphibole (10.5–15.4 wt.% CaO and 2.9–5.1 wt.% TiO_2) is very close to the results from Grützner et al. (2013) and is best described as Fe-bearing kaersutite (Table 3). With increasing temperature, there is a slight increase in Na_2O content and Mg# and a slight

decrease in TiO_2 concentration. On the other hand, phlogopite exhibits low TiO_2 values at subsolidus conditions (2.3–2.6 wt.%) and elevated TiO_2 at higher temperatures (3.8–5.2 wt.%). The increased TiO_2 concentrations are coupled with a slight Mg- and Fe-decrease in phlogopite, which buffers the Mg# and keeps it constant at 88–89 (Table 3).

Minor phases

Rhönite ($Ca_2(Mg,Fe^{2+})_4TiFe^{3+}[O_2|Al_3Si_3O_{18}]$) is a stable subsolidus phase at 1 GPa and 1000 °C together with plagioclase, small amounts of calcite, Mg-ilmenite and ulvöspinel. At 1 GPa and 1100 °C, only rhönite remains stable together with kaersutite (Fig. 2). Both melt-out between 1100 and 1150 °C. Rhönite composition is listed in Table 3. At 3 GPa and 1100 °C the metasome contains Cr-spinel and Mg-ilmenite. They break down at around 1150 °C but appear due to a slight temperature gradient in the coolest regions of capsule E150.

Melt composition

The melts produced have a range of compositions from ultrabasic (< 45 wt.% SiO_2) to basic (45–52 wt.% SiO_2). At 1 GPa, the highest SiO_2 content is observed at 1100 °C, with 49.0(5) wt.%. On the other hand, E182 (4 GPa, 1200 °C) has the lowest SiO_2 content of 29(1) wt.%, followed by E150 (3 GPa, 1150 °C) and E177 (3 GPa, 1200 °C) with 32.8(4) and 33.5(8) wt.% SiO_2, respectively. The "only-metasome" experiments have intermediate SiO_2 contents of 40.3(2) wt.% at 1100 °C and 41.0(3) wt.% at 1200 °C.

Na_2O content of the experimental melts ranges up to 4.9(5) wt.% in E157 and 4.9(8) wt.% in E177. Both represent low-temperature melts at 1 and 3 GPa. As the temperature increases, the Na_2O concentration decreases, reaching 2.5(2) wt.% in E166. All melts are sodic, with a ratio of $K_2O/Na_2O \leq 1$. The only exception is the lowest temperature melt at 4 GPa (E182), which is potassic with a K_2O/Na_2O ratio of 1.3(3).

All microprobe analyses of the melts have totals below 100 wt.% due to the volatile content of the metasome starting material. Depending on the melt fraction, totals range from 83(1) wt.% to 95(1) wt.%. $CaCO_3$ can be found subsolidus at 1 GPa in the metasome starting material (Grützner et al. 2013) suggesting that CO_2 is a relevant volatile component, in addition to water from hydrous phases like amphibole and phlogopite.

The melts exhibit strong enrichment in most of the analyzed trace elements, particularly large-ion lithophile elements (LILE), high-field-strength elements (HFSE), and light rare-earth elements (LREE). Conversely, melts at 3 and 4 GPa show slight depletion in heavy rare-earth elements (HREE) due to the presence of garnet in the residuum. The trends of enrichment and depletion become more pronounced with increasing pressure and smaller with increasing temperature/increasing melt fraction (see Fig. 4). The concentrations of trace elements closely resemble the average Kula basanite values (Grützner et al. 2013) and follow the trend of average low silica Ocean Island Basalt. Furthermore, experiments at 1 GPa exhibit slight depletion in trace elements relative to experiments at 3 and 4 GPa.

Discussion

Evolution of melt compositions from experiments

In the experiments conducted at different pressures, two types of assemblages were observed: those containing subsolidus phases without melt, and those with the presence of the melt phase. By considering both types of runs, the solidus temperature can be approximately determined. It shifts with increasing pressure, ranging from 1075 ± 25 °C at 1 GPa to 1125 ± 25 °C at 3 GPa, and further increasing to 1175 ± 25 °C at 4 GPa for the reaction experiments. It's worth noting that in *only-metasome experiments* at 1 GPa, the solidus appears to be at a slightly lower temperature. The uncertainty of the solidus is given by the experimental temperature brackets of 50 °C between subsolidus runs and the first run that contains melt in the samples. It has also to be noted that the first phase to melt is probably not amphibole but minor phases like small amounts of carbonates from the metasome (Grützner et al. 2013) or Mg-ilmenite at 4 GPa which was found subsolidus and can explain the high TiO_2 content in the initial 4 GPa melt.

1 GPa reaction runs

The reaction-experiments at 1 GPa are dominated by the decline of amphibole until additional clinopyroxene melting starts between 1150 and 1200 °C (Fig. 2, Figure S5). First melting occurs at 1100 °C and the analyzed low-degree melt (E157) is extraordinarily rich in SiO_2 and Al_2O_3, but it is still silica undersaturated (Figure S6) with the Q parameter [normative q − (ne + lc + kls)] ranging from > −10 to −17 (Figure S7), resembling overall a phonotephritic composition. The low FeO values in E158 are due to the capsule material, while Pt was used which is known for Fe

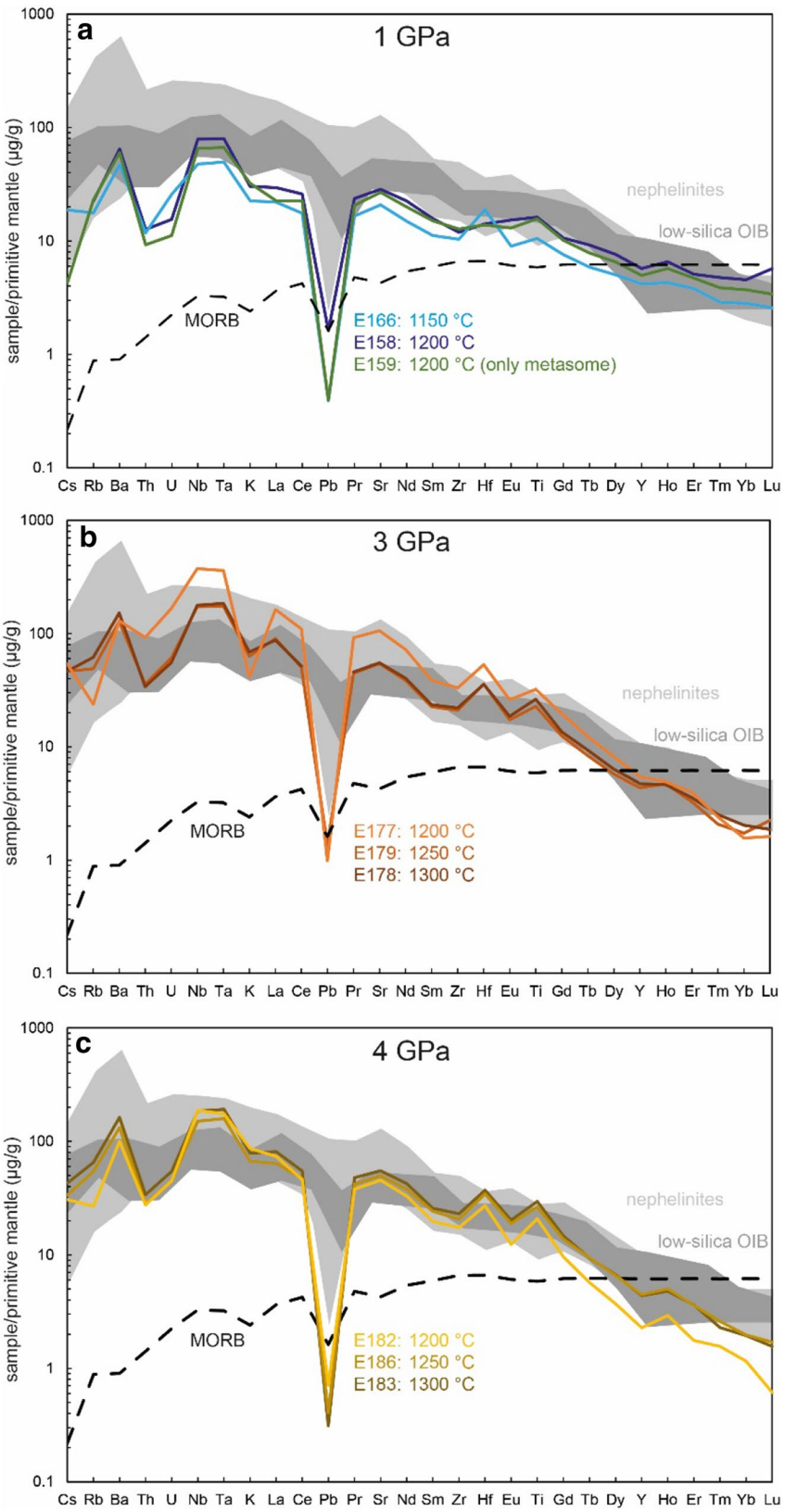

Fig. 4 Trace element concentrations normalized to primitive mantle are close to the average low silica Ocean Island Basalt (OIB) trend. High fraction melt experiments (≥ 1150 °C) at 1 GPa are slightly depleted in trace elements relative to the OIB trend and to experiments at 3 and 4 GPa. The melt at 3 GPa and 1200 °C is slightly enriched in trace elements relative to melts at 1250 and 1300 °C with higher melt fraction. The grey field shows average low-silica OIB and was compiled by Pilet et al. (2008) from the GEOROC database (https://georoc.eu/) and from PetDB (http://www.earthchem.org/petdb). Primitive high pressure nephelinite melts (MgO values between 8 and 15 wt.% and Dy/Yb ratios > 3.5) are taken from a precompiled dataset from the GEOROC database (DIGIS Team 2022)

consumption during long-lasting experiments (e.g., Wang et al. 2020), instead of AuPd. Generally, our experiments demonstrate that Q is strongly pressure-dependent, with decreasing values from low to high pressure. In the case of 1 GPa experiments, high SiO_2 and Al_2O_3 contents can be best explained with the breakdown instead of melting of amphibole: its decompression breakdown produces rhönite and triggers partial melting that produces a phonotephritic melt. The amphibole (kaersutite) stability field and the melt generation by decompression breakdown of kaersutite will be addressed in more detail further below.

1 GPa only-metasome experiments

The change in melt composition for the two *only-metasome experiments* shows a shift from amphibole-dominated melting at 1100 °C to amphibole + clinopyroxene melting at 1200 °C. In both cases, amphibole melts incongruently to produce olivine+clinopyroxene+melt at 1150 °C, and olivine (only)+melt at 1200 °C. The melt composition remains close to the analyzed amphibole composition, even at 1200 °C, when about half of the capsule is filled with melt (Fig. 2).

Reaction-experiments at 1150 and 1200 °C and only-metasome runs at 1100 and 1200 °C show some differences in major element concentration: the melts produced by 1 GPa only-metasome experiments at 1200 °C have elevated Na_2O, K_2O, CaO, and much higher FeO values, but lower Al_2O_3, SiO_2, MgO, and MnO concentration compared to reaction experiments. The compositional differences in element concentration between the reaction-experiments and only-metasome runs must be explained by the reaction with lherzolite. Calcium for example, can be buffered by clinopyroxene and orthopyroxene from the lherzolite and should be therefore lower in the reaction melt as lherzolite pyroxenes take up CaO. This is in good agreement with similar findings in literature: in melt-rock reaction experiments between basalt and peridotite van den Bleeken et al. (2010) observed at 1230 °C and 0.8 GPa an CaO uptake by the peridotite and a transformation into wehrlite.

The two types 1100 °C experiments show larger differences, as in the reaction runs only a fraction of the amphibole breakdown products is melting. Rhönite is still stable. Therefore, the reaction experiments have higher alkali concentration than the only-metasome experiments.

3 and 4 GPa experiments

As pressure increases, the concentrations of SiO_2 and Al_2O_3 in the melt decrease, along with the parameter Q (Figure S7), while TiO_2, MgO, and MnO slightly increase compared to melts produced in the 1 GPa experiments (Fig. 5). These differences are attributed to the presence of two phases that are not stable at 1 GPa: (1) phlogopite and (2) garnet.

(1) At 3 GPa phlogopite and amphibole are the stable hydrous phases. At 4 GPa only minor amounts of amphibole were found at the subsolidus. Amphibole breaks down first but phlogopite follows quickly between 1200 and 1250 °C. Therefore, runs at 3 and 4 GPa show nearly parallel temperature trends for major and minor element composition (except Na; Fig. 5) with 4 GPa runs being generally higher than 3 GPa runs in CaO, TiO_2, MgO and FeO, but lower in Al_2O_3, MnO and SiO_2. Na_2O and K_2O show different concentrations at 1200 °C but become nearly identical for 3 and 4 GPa at higher temperatures (Figure S6). The Na_2O/K_2O ratio of the melt increases due to amphibole melting until a maximum is reached at 1200 °C and 3 GPa (Na_2O/K_2O 3.8 ± 3.0). As the temperature increases further, Na_2O/K_2O decreases again when phlogopite ($Na_2O/K_2O < 0.1$) melts-out. Clinopyroxene remains stable or does not melt to significant amounts in this temperature range (Figure S5).

It has to be noted that the metasome starting material does not contain any phlogopite (Grützner et al. 2013). Additionally, experiments at 4 GPa were not necessarily designed to reproduce a natural system, but rather to demonstrate the effect of pressure on the melt-rock reaction. Nevertheless, the presence of phlogopite in 3 and 4 GPa experiments influences the composition of the low-fraction melts at these pressures. In these experiments, phlogopite crystallized from a phlogopite-free, amphibole-rich starting material, and as the melt fraction increases, the melt composition becomes more amphibole-like. This is essential to consider because melts derived from phlogopite-rich metasomes, such as glimmerite, are likely to form ultrapotassic melts (Förster et al. 2017). The phlogopite composition from our experiments and Förster et al. (2017) demonstrates some resemblances. However, the glimmerite starting material from Förster et al. (2017) has more SiO_2 (47.37 vs. 41.9 wt.%), much more K_2O (8.03 vs. 0.77 wt.%), less FeO (6.29 vs. 9.7 wt.%), and less CaO (6.47 vs. 12.6 wt.%). The phlogopite mineral fraction in the starting material of Förster et al. (2017) is much higher than the amount of phlogopite observed subsolidus in our experiments at 3 and 4 GPa.

(2) Garnet was found in all experiments at 3 and 4 GPa, and it remains stable even at the highest run temperature (1300 °C). The presence of garnet likely causes the major difference in melt composition between 1 GPa experiments and 3–4 GPa experiments. At 1 GPa, only clinopyroxene and olivine remain as residual phases coexisting with the melts. In contrast, at 3 and 4 GPa, residual garnet binds SiO_2

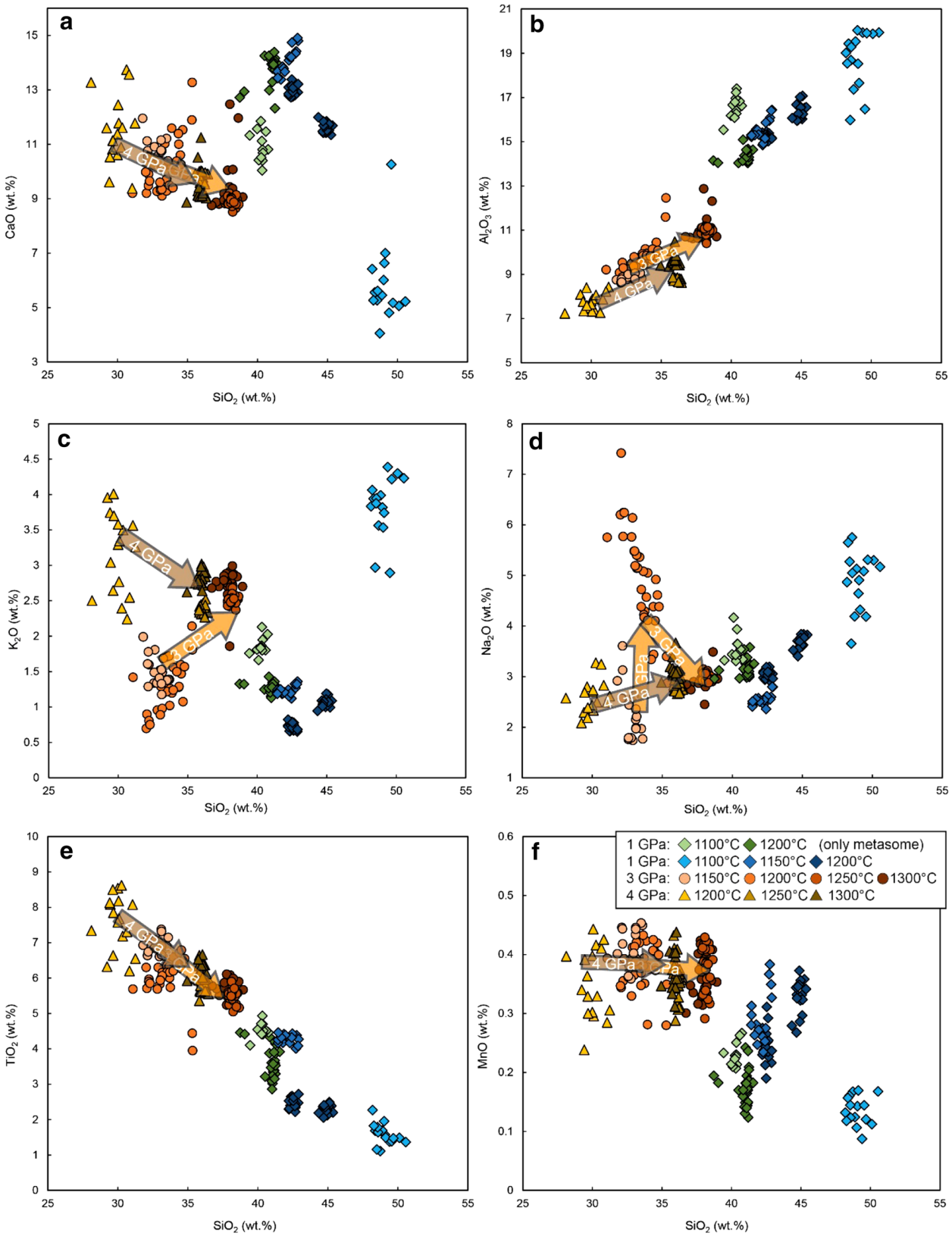
a
CaO (wt.%)
SiO2 (wt.%)
4 GPa
3 GPa
b
Al2O3 (wt.%)
SiO2 (wt.%)
3 GPa
4 GPa
c
K2O (wt.%)
SiO2 (wt.%)
4 GPa
3 GPa
d
Na2O (wt.%)
SiO2 (wt.%)
3 GPa
4 GPa
e
TiO2 (wt.%)
SiO2 (wt.%)
4 GPa
3 GPa
f
MnO (wt.%)
SiO2 (wt.%)
4 GPa
3 GPa
1 GPa: 1100°C 1200°C (only metasome)
1 GPa: 1100°C 1150°C 1200°C
3 GPa: 1150°C 1200°C 1250°C 1300°C
4 GPa: 1200°C 1250°C 1300°C

◂**Fig. 5** Major and minor oxide concentration of experimental glasses at 1, 3 and 4 GPa. Arrows indicate the temperature trends for melt evolution at 3 and 4 GPa. 1 GPa reaction-experiments have elevated Na_2O, Al_2O_3, SiO_2 and MgO, but lower CaO, TiO_2 and much lower FeO values compared to only-metasome runs. 3 and 4 GPa show nearly parallel temperature trends for major and minor element composition with 4 GPa runs being generally higher than 3 GPa runs in CaO, TiO_2, MgO and FeO, but lower in Al_2O_3, MnO and SiO_2. The differences in melt composition are caused by the two phases that are not stable in 1 GPa experiments: phlogopite and garnet

and Al_2O_3, as well as HREE, resulting in the corresponding melts being more Si-undersaturated and more nephelinitic (Fig. 6) with a larger extent of REE fractionation (Fig. 4).

The formation of garnet in SiO_2-undersaturated systems is also linked to the dissolution of orthopyroxene and the formation of clinopyroxene (O'Hara 1968). Alkaline basalts as well as tholeiites are undersaturated in pyroxene at low pressure. These melts react with enclosing peridotite during the melting process, or during their transport to the surface and produce orthopyroxene dissolution which has been confirmed in many studies (e.g., Daines and Kohlstedt 1994; Kelemen et al. 1995; Lundstrom et al. 2000; Morgan and Liang 2005; Van den Bleeken et al. 2011). It is intriguing to assume a higher concentration of residual clinopyroxene at 4 GPa experiment compared to lower pressures. Clinopyroxene has a higher SiO_2 content than garnet or phlogopite and more clinopyroxene in the residuum could well explain the shift of melt composition. However, the calculated modal abundances do not show a strong increase of clinopyroxene at high pressure—for comparable amounts of melt (Supplementary Table S1).

Pressure–temperature stability of kaersutite and its breakdown behaviour

In our experiments, kaersutite (Ti-rich Ca-amphibole) was observed at 1, 3, and 4 GPa, but its stability is limited at 4 GPa, being significant only at subsolidus temperatures ($T < 1200$ °C). The stability of amphiboles is known to be strongly influenced by the chemical composition of the host rock: Mandler and Grove (2016) found pargasite (Ca-amphibole) to be stable up to 3.8 GPa, indicating that amphibole can persist at higher pressures in fertile peridotites compared to depleted ones. Studies by Niida and Green (1999) demonstrate that pargasite remains stable up to 1150 °C and 3 GPa in MORB compositions, and the breakdown reaction depends on the amphibole composition and occurs over a wide range of pressures and temperatures.

With increasing temperature, amphibole breaks down incongruently following the reaction: amphibole±clinopyroxene = olivine+melt. At a pressure below 1 GPa pargasite and kaersutite can not only melt due to heating but also by decompression (e.g., Niida and Green 1999; Shaw 2009). The melting temperatures of the decompression breakdown components of pargasite range from 950 to 1100 °C (Niida and Green 1999) and is likely to be similar for kaersutite. In field samples of Kula metasomes, several kaersutite grains were found with decompression breakdown corona or resorption zone containing olivine+clinopyroxene+rhönite+spinel±plagioclase±glass (Grützner et al. 2013). The same mineral composition can be found in our experiments at 1 GPa and 1000–1100 °C (Fig. 2a). Kaersutite is not stable at 1 GPa and 1000 °C in the experimental system, and instead, spinel+rhönite+plagioclase can be found. In fact, kaersutite is present in a small area at the rim of the capsule in a run at 1100 °C which is probably due to small thermal gradients in the capsule and the temperatures may have been slightly lower than 1100 °C. At 1100 °C rhönite is still present together with glass patches, but plagioclase and spinel disappear (Fig. 2b). The presence of residual rhönite together with the inception of kaersutite melting produce a small amount of phonotephritic melt (Fig. 2b). With further temperature increase, the melting of rhönite and kaersutite results in an increasing melt fraction that becomes basaltic or basanitic at 1150–1200 °C, after all breakdown products except clinopyroxene and olivine melted (Fig. 6).

Based on these observations, we propose that the formation of the "evolved" phonotephritic melt at 1100 °C and 1 GPa can be best explained by the partial melting of amphibole breakdown products. The implications of generating slightly evolved, but still Si-undersaturated melt from metasome melting for alkaline volcanism on a thin lithosphere, such as the Kula volcanic province, will be discussed further below.

Rhönite is mainly known as a secondary phase that forms during the breakdown of Ti-rich phases like kaersutite (Kunzmann 1999). Although data about this phase in igneous rocks is limited, rhönite is known to be stable within a narrow pressure–temperature range (< 0.06 GPa and 840–1200 °C) in ultramafic systems and at pressures of < 0.5 GPa and temperatures of 1180–1260 °C in olivine melt inclusions of alkaline rocks (Sharygin et al. 2011). Rhönite has been used to roughly constrain eruption temperature or crystallization conditions of alkaline lavas (Sharygin et al. 2011; Grützner et al. 2013).

However, our experiments show that rhönite can be stable at pressures exceeding 1 GPa and at temperatures between 1000 and 1100 °C, which aligns well with the temperature range constrained by Kunzmann (1999) and Sharygin et al. (2011). From our experimental findings, we argue that the

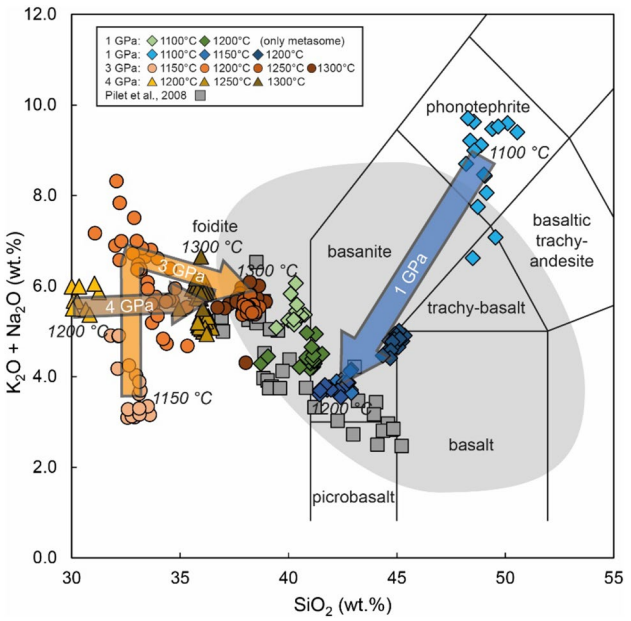

Fig. 6 Total alkalis vs. SiO_2 of experimental glasses show different temperature trends (arrows) for 1, 3 and 4 GPa with increasing temperature. First melts at 1 GPa are phonotephritic and become basanitic at higher temperatures due to different amphibole melting mechansims. Melts at 3 and 4 GPa are nephelinitic and become slightly richer in SiO_2 with increasing temperature. The grey field represents ocean island basalts, Hawaiian shield stage basalts, and Iceland basalts with 8–15 wt.% MgO and $Na_2O/K_2O < 0.8$ compiled by Pilet (2015) from the GEOROC database (https://georoc.eu/) and from PetDB (http://www.earthchem.org/petdb)

pressure–temperature stability range of rhönite warrants further investigation, and PT constraints of rhönite-bearing rocks should be treated with caution.

Wehrlitization

At subsolidus conditions from 1 to 4 GPa, the lherzolite is poorly crystallized and shows no compositional reaction front in the contact zone with the metasome, unlike reaction experiments where eclogites (Mallik and Dasgupta 2012; Gervasoni et al. 2017) or glimmerites (Förster et al. 2017) are involved together with peridotite. The first reaction between both lithologies in the capsule occurs in the presence of melt. The initial melting is primarily generated in the metasome and situated in the metasome or at the capsule wall. Even at low melt fractions (Fig. 1d), the melt is highly mobile, similar to processes observed in other melting- and melt extraction phenomena, such as during eclogite melting (Kogiso et al. 2004).

Once the melting starts, the metasome-derived melt interacts with the lherzolite leading to consumption of orthopyroxene. The remaining residue at 1 GPa is a crystal mush of olivine and clinopyroxene, and no Al-bearing phase remains stable at $T > 1150$ °C, whereas at 3 and 4 GPa, garnet is stable together with olivine and clinopyroxene, resulting in the formation of a wehrlitic residue. It has to be noted that the two processes of metasome-melting and reaction with the peridotite can be decoupled in nature. The melt-mantle interaction can occur during the melt percolating the lithosphere, forming wehrlitic channels. In such cases, the composition

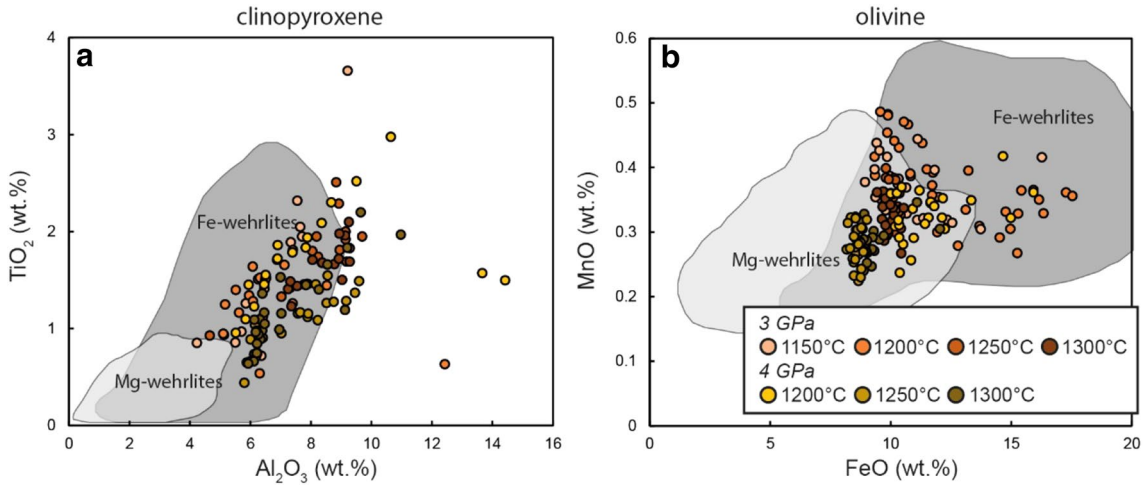

Fig. 7 Element composition of clinopyroxene and olivine in wehrlitic residues. The grey fields represent global wehrlite composition of Mg-wehrlites and Fe-wehrlites compiled from various studies by Patkó et al. (2020, references therein). **a** The majority of clinopyroxene analyses lie in the field of Fe-wehrlites. Some samples have slightly higher Al_2O_3 contents. **b** olivine values lie in the overlapping area of Mg- and Fe-wehrlites

of the magmas produced after the reaction could be slightly different from the one predicted by our experiments, as the mantle would then represent an almost infinite reservoir. To study this effect, a different experimental setup would be required, such as significantly reducing the metasome component as described in the layered experiments by Pilet et al. (2008) or focusing on a melt-rock reaction (e.g., van den Bleeken et al. 2010).

A lherzolite-wehrlite transformation is typically caused by either silicate or carbonate melts as a metasomatic agent (e.g., Rudnick et al. 1993; Shaw et al 2005; Yaxley et al. 1991, 1998; Zinngrebe and Foley 1995). As mentioned above, it is unlikely that fluid-rock interaction can cause this transformation and a supercritical CO_2-rich fluid (Yaxley et al. 1991) can be excluded. Besides two outliers, our calculated CaO/Al_2O_3 ratios (0.8–4.7; Figure S3) can also be used to argue against CO_2-dominated metasomatism (> 5 expected) and we find that our data support metasomatism with a mafic melt (after Yaxley et al. 1991). Supersolidus clinopyroxenes in both lherzolite and metasome have about the same high CaO content as subsolidus clinopyroxene in the metasome (Figure S3) and show no compositional differences between former metasome and former lherzolite. Both olivine and clinopyroxene have low Mg# < 90. These Mg# are expected for the formation of Fe-wehrlites while carbonate metasomatism instead has typically Mg# > 90 (Mg-wehrlites; Yaxley et al. 1991). Comparing wehrlite olivine and clinopyroxene composition from our experiments with worldwide wehrlites compiled by Patkó et al. (2020), olivine lies well in the field of Fe-wehrlite while some clinopyroxenes from this study have a slightly higher Al_2O_3 concentration than natural wehrlites (Fig. 7).

Our experiments show that alkaline magma formation by amphibole-rich metasome melting can transform lherzolite into wehrlite and that the wehrlitization connected to alkaline volcanism does not require additional separate metasomatic processes but can be linked directly to the alkaline magma generation.

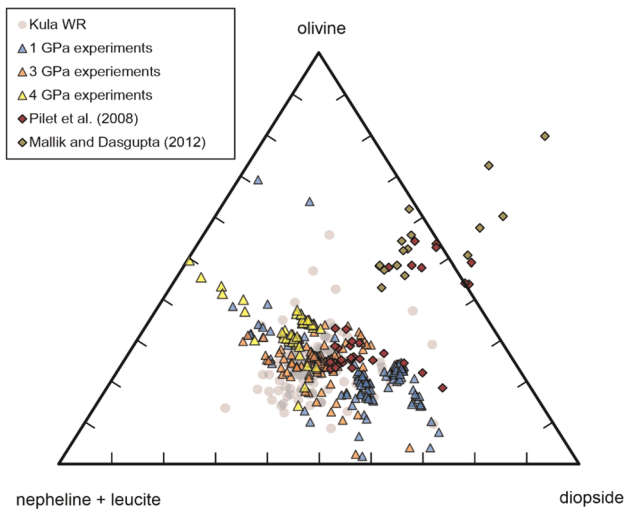

Fig. 8 Normative bulk rock/experimental glass composition in the triangular plot olivine vs. diopside vs. nepheline+leucite. The data outside this triangle are hypersthene normative. All experimental glasses from this study are nepheline normative. While other studies (Mallik and Dasgupta 2012; Pilet et al. 2008) find a clear difference between the reaction potential with lherzolite and the normative nepheline content, the effect cannot be observed in glasses from this study. Kula whole rock data: Aldanmaz (2002), Aldanmaz et al. (2015), Alıcı et al. (2002), Chakrabarti et al. (2012), Dilek and Altunkaynak (2010), Grützner et al. (2013), Güleç (1991), Nikogosian et al. (2018), Notsu et al. (1995) and Tokçaer et al. (2005). See also Supplementary Table S2 for Kula lavas from literature

Alkaline melt generation from metasome-mantle experiments

Traditional experimental petrology has shown that alkaline magmas can be generated by low degree melting of peridotite at great depths, whereas sub-alkaline rocks are most likely derived from shallower regions and are formed by higher degrees of melting (e.g., Green and Ringwood 1967; Green 1973). The partial melting experiments of a nominally dry peridotite at various pressures (1–7 GPa) demonstrate that at relatively low pressure (1–1.5 GPa, e.g. Wasylenki et al. 2003) the produced melts will compositionally resemble MORB-like tholeiites, whereas alkaline melts with intermediate SiO_2 content (~ 45 wt.%) will be generated by lower degrees of partial melting at asthenospheric depths (> 3 GPa). However, the experiments failed to produce Si-undersaturated alkaline basalts even at incipient partial melting conditions (Davis and Hirschmann 2013; Davis et al. 2011). Moreover, the compositional continuum from nephelinites and basanites to alkali olivine basalts and tholeiites universally observed in many intraplate volcanoes that have been interpreted as an increase in the degree of partial melting of a common mantle source has never been experimentally reproduced (c.f. Fig. 8 and Figure S7). This implies that ultrabasic alkaline magmas such as nephelinite and phonotephrite cannot be produced solely from four-phase peridotite, and some alternative models need to be considered. Several authors proposed that alkaline magmas, which are silica-undersaturated and enriched in incompatible trace elements may either be formed by the melting of peridotite in the presence of CO_2 (Hirose 1997; Dasgupta and Hirschmann 2007; Dasgupta et al 2007), by reaction of melt from different lithologies (e.g. eclogite, pyroxenite)

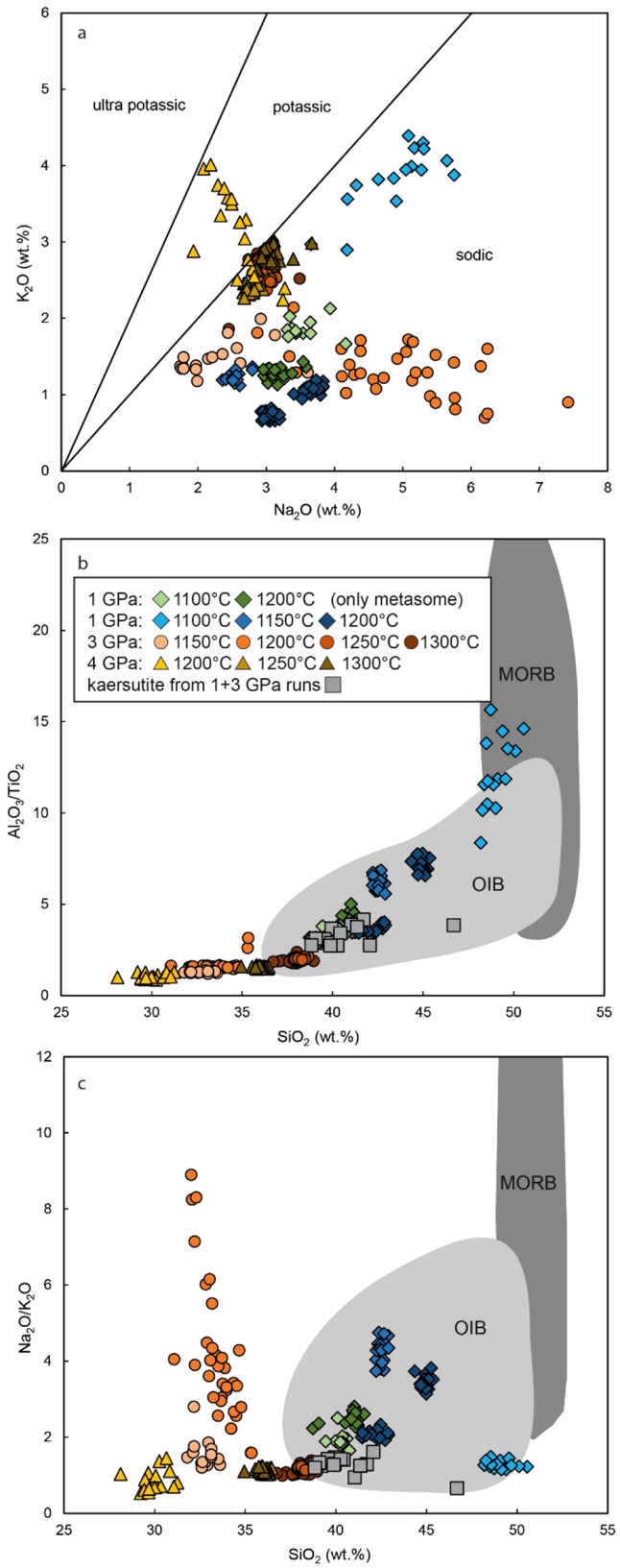

Fig. 9 Major and minor oxide ratios of experimental glasses at 1, 3 and 4 GPa. **a** K_2O vs Na_2O in experimental glasses show that most melts are sodic. Only E182, the first melt at 4 GPa (1200 °C) is potassic. **b**, **c** 1 GPa glasses and high melt fraction glasses at 3 GPa runs overlap with worldwide OIB values and worldwide amphiboles from metasomes, both shown in the light grey field (Pilet 2015). Amphiboles from experiments show good matching with glasses and OIB. The OIB and MORB dataset were compiled by Pilet (2015) from the GEOROC database (https://georoc.eu/) and from PetDB (http://www.earthchem.org/petdb)

with surrounding peridotite (Hirschmann et al. 2003; Kogiso et al. 2003; Mallik and Dasgupta 2012), or by melting of the metasomatized lithosphere (Halliday et al. 1995; Niu and O'Hara 2003; Pilet et al. 2008; Pilet 2015). Importantly, only the experiments on metasomatized peridotites, including ours, have generated nepheline normative rocks that resemble also alkaline lavas in terms of enriched trace element patterns (Pilet et al. 2008; Pilet 2015).

Figure 6 shows the range of worldwide primitive ocean island basalts (OIB) including data from Hawaiian shield stage basalts and Iceland basalts compiled by Pilet (2015) from the GEOROC database (https://georoc.eu/) and PetDB (http://www.earthchem.org/petdb). High fraction melts at 1 and 3 GPa from our experiments at the stage of fully molten amphibole plot within the field of OIB. The low-melt fraction experiments plot close to OIB composition, as well as 4 GPa runs. According to the alkali contents of our experiments, we can constrain the formation of OIB-like melts to 3 GPa > 1200 °C. Note that 4 GPa runs at $T > 1300$ °C would not necessarily meet the OIB field as both the bulk lherzolite and metasome composition do not plot within the field. All our melts are sodic ($K_2O < Na_2O$) except in the experiment with the lowest melt fraction at 4 GPa (Fig. 9), which is potassic ($K_2O > Na_2O$). The melts overlap with alkali basalts in a total alkali vs. silica diagram and plot in the fields of nephelinite, basanite, and phonotephrite (Fig. 6).

The trace element compositions of our experimental melts show a typical OIB signature for low-Si alkaline lavas with high contents of very incompatible trace elements (Fig. 4), ratios of Rb/Ba, K/Nb and Pb/Ca that are < 1 (c.f. Table 6), and a typical decreasing HREE slope showing an enrichment between 10 and 1 relative to the primitive mantle (Fig. 4). They have MgO values between 9.2 and 14.3 wt.% which makes them potential candidates for primary magmas. Only the melts at 1 GPa and 1100 and 1150 °C have lower MgO content with 5 and 7.3 wt.%, respectively.

In the majority of alkaline rocks, Al_2O_3/TiO_2 and Na_2O/K_2O are < 10 independently of the SiO_2 content. These ratios in the lavas overlap the ones in amphiboles from metasomatic veins worldwide, which is another supporting argument for the generation of alkaline rocks from amphibole-bearing metasomatic assemblages (Pilet 2015). Amphiboles and glasses from our experiments confirm this as Al_2O_3/TiO_2 in glasses from this study range from 0.9 to 7.5 in the 3 GPa, with the 4 GPa low melt fraction experiments having the lowest values and the 1 GPa melts having the highest values. Only the lowest melt fraction at 1 GPa (1100 °C) has higher Al_2O_3/TiO_2 between 8.4 and 15.8. Na_2O/K_2O is in the range of 0.8–4.8 with no clear pressure or temperature trend (Fig. 9). Amphiboles in our experiments match with the corresponding melts and have values of $Al_2O_3/TiO_2 = 1.4–3.5$ and $Na_2O/K_2O = 1.3–1.4$ for kaersutite amphibole. Representative kaersutites from the starting material metasome have values of $Al_2O_3/TiO_2 = 3.3$ and $Na_2O/K_2O = 1.5$ (Grützner et al. 2013).

Within their experiments, Pilet et al. (2008) observe some impact of the experimental setup for the melt composition: pure metasome melting experiments generate melts that are rich in normative nepheline, while sandwich layer reaction experiments with lherzolite produce melts that are less nepheline normative and contain more SiO_2. Mallik and Dasgupta (2012) synthesized OIB melts from reaction experiments between volatile-free MORB-eclogite and volatile-free fertile peridotite and find an opposing trend: in a setup with high wall rock-reaction potential, the melts become alkaline while with less wall rock reaction potential the melts trend to become tholeiitic. In our study, we do not find any significant difference between only-metasome and reaction experiments, but to affirm this observation a larger data set of only-metasome experiments is needed.

Implications for alkaline volcanism erupted on thin delaminated lithosphere from 1 GPa experiments: the Kula volcanic province

The Kula volcanic province is located in Western Anatolia and represents the youngest volcanic activity in this region. ^{3}He exposure dating of some well-preserved lava flows yields an age of 0.9 ± 0.2 ka (Heineke et al. 2016). The Kula Na-alkaline lavas have an anorogenic geochemical signature similar to other intraplate volcanic provinces within the Circum-Mediterranean region (Lustrino and Wilson 2007), suggesting that they are derived from the asthenospheric mantle. They are unique in Western Anatolia as they are surrounded by widespread Cenozoic orogenic potassium-rich magmatism.

Traditionally, the origin of Kula magmatism has been linked to lithospheric delamination and the upwelling of asthenospheric material through a slab window (e.g., Chakrabarti et al. 2012; Prelević et al. 2012, 2015). However, there is a significant time gap between the lithosphere delamination that affected this part of Western Anatolia around 20 Ma (e.g. Prelević et al. 2012; Nikogosian et al. 2018) and the major episode of Kula volcanism at less than 1.7 Ma (Richardson-Bunbury 1996). To explain this delay, Nikogosian et al. (2018) argue that the Kula magmatism is driven by a recent mini-plume.

The findings from the 1 GPa experiments offer an alternative explanation for this delay. Applying the alkaline melt generation model from Pilet (2015), the continuous rise of

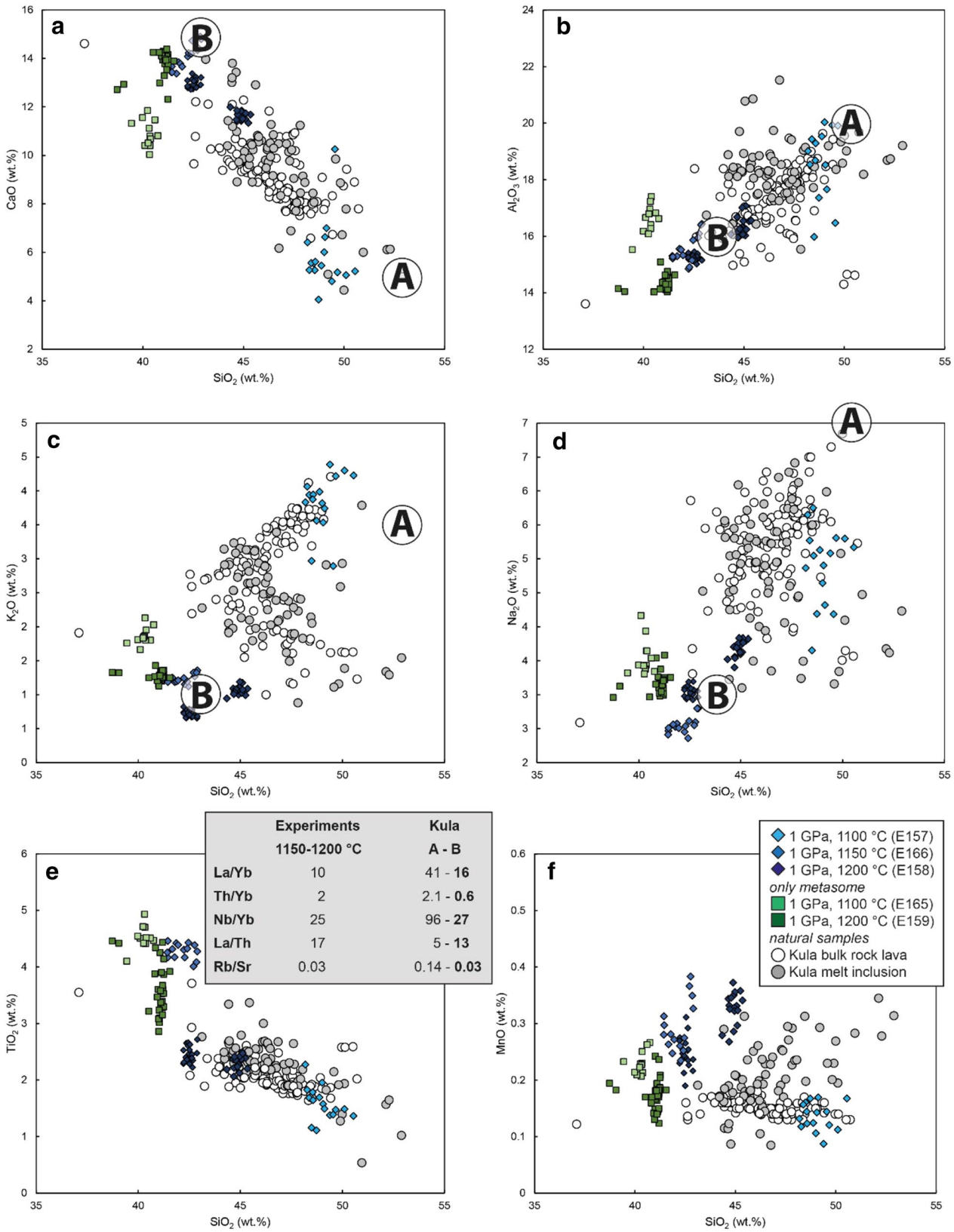
a
CaO (wt.%)
SiO2 (wt.%)
B
A
b
Al2O3 (wt.%)
SiO2 (wt.%)
A
B
c
K2O (wt.%)
SiO2 (wt.%)
A
B
d
Na2O (wt.%)
SiO2 (wt.%)
A
B
e
TiO2 (wt.%)
SiO2 (wt.%)
Experiments 1150-1200 °C
Kula A - B
La/Yb 10 41 - 16
Th/Yb 2 2.1 - 0.6
Nb/Yb 25 96 - 27
La/Th 17 5 - 13
Rb/Sr 0.03 0.14 - 0.03
f
MnO (wt.%)
SiO2 (wt.%)
1 GPa, 1100 °C (E157)
1 GPa, 1150 °C (E166)
1 GPa, 1200 °C (E158)
only metasome
1 GPa, 1100 °C (E165)
1 GPa, 1200 °C (E159)
natural samples
Kula bulk rock lava
Kula melt inclusion

◂**Fig. 10** Major and minor element oxides vs SiO_2 of 1 GPa experiments, and natural Kula samples show a two component mixing trend between amphibole melting (E166, E158, E165, E159) and amphibole breakdown product melting (E157). The mixing endmember A and B (Nikogosian et al. 2018) close to experimental melts at 1100 °C for most elements, the endmember B agrees very well with amphibole melting experiments at 1150 and 1200 °C. Data sources for Kula bulk rock lava are from Aldanmaz (2002), Aldanmaz et al. (2015), Alıcı et al. (2002), Chakrabarti et al. (2012), Dilek and Altunkaynak (2010), Grützner et al. (2013), Güleç (1991), Nikogosian et al. (2018), Notsu et al. (1995) and Tokçaer et al. (2005). Olivine melt inlcusion data are from Nikogosian et al. (2018). See also Supplementary Table S2 for Kula lava

asthenospheric precursor (low-fraction) melts forms metasomatized zones in the lithosphere that are rich in kaersutite and diopside bearing metasomes. The continuous addition of hydrous material alters the thermal gradient until kaersutite melts at a critical temperature and generates alkaline Kula magmatism with some delay compared to the fertile asthenospheric melts. This process may act as a trigger and can be repetitive, contributing to the intermittent volcanic activity observed.

To generate alkaline melts from amphibole metasomes at 1.5–2.5 GPa, Pilet (2015) expects a melting temperature of about 1150–1175 °C which is much lower than temperatures needed for low-degree asthenospheric melting. Given a crustal thickness of about 30 km below Kula (Saunders et al. 1998; Holness and Bunbury 2006; Karabulut et al. 2019) a pressure of about 1 GPa can be expected at the uppermost lithosphere and slightly lower melting temperatures. Nikogosian et al. (2018) calculated 0.9–2.3 GPa for the Kula magma source and 1215–1415 °C for the melt generation by a mini plume. Full amphibole melting happened in our experiments at ≥ 1 GPa and 1100–1150 °C. Low-pressure amphibole breakdown with melt formation can be expected from our experiments at conditions ≤ 1 GPa and 1000–1100 °C. The continuous addition of metasomatic material will not only cause amphibole melting at > 1100 °C but also low-pressure amphibole breakdown in a slightly colder regime. The melts that form during amphibole breakdown are richer in SiO_2 than the slightly hotter alkaline melts but can be assumed to be mobile (e.g., Kogiso et al. 2004). Mixing these two types of melts during their ascent is a highly likely scenario.

The phonotephrite melt generation from amphibole breakdown products pressure–temperature conditions requires a relatively steep geothermal gradient and a thin lithosphere. To our knowledge the lithosphere-asthenosphere boundary is not well constrained below Kula, but it has been reported that the lithosphere below Western Anatolia in general is anomalously thin (50–80 km) and hot (Artemieva and Shulgin 2019; Mahatsente et al. 2017, Salaün et al. 2012). We can speculate that appearance of melts that form during amphibole breakdown denote a stage when the lithosphere has been further delaminated below Kula most recently. At that stage, the lithosphere just reaching approximate thickness when the slightly hotter alkaline melts derived from the asthenosphere will trigger amphibole breakdown within the lithosphere.

The origin of alkaline melts as the mixing of two or more different chemical endmembers is strongly supported by findings in olivine melt inclusion (Nikogosian et al. 2018).

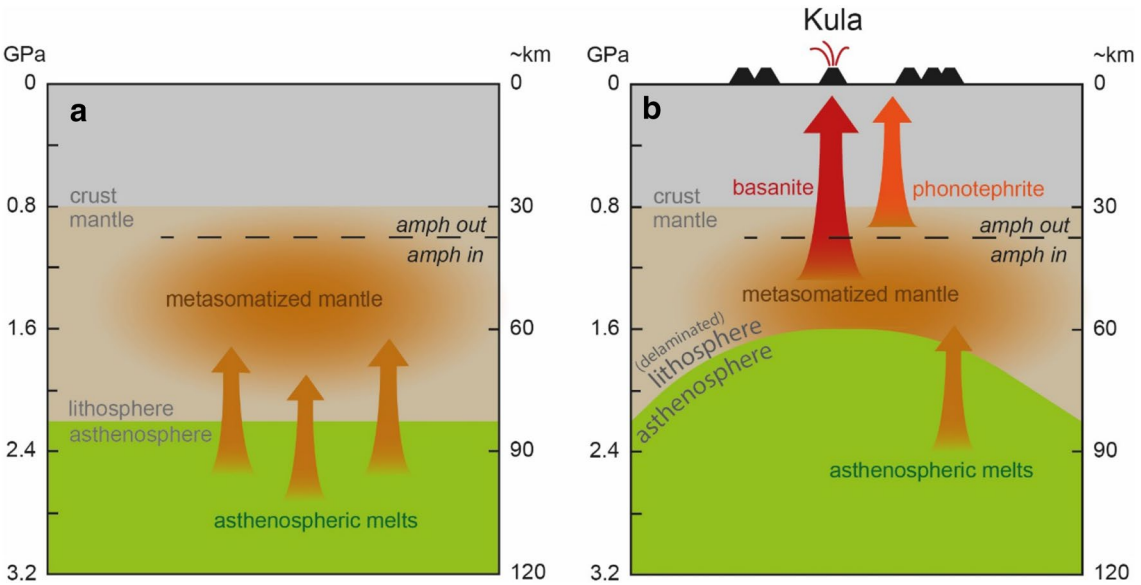

Fig. 11 Metasome melting model for the Kula volcanic province. **a** Astenosphere-derived precursor melts produce a metasomatized mantle. **b** The metasomes melt when the thermal gradient increases due to e.g., further crustal delamination and ongoing metasomatism lowers the solidus and trigger alkaline volcanism (c.f. Pilet 2015). Amphibole melting causes basanitic melts (red arrow). The melting of decompression amphibole breakdown products generates phonotephritic melts (small orange arrow). Mixing of basanite and phonotephrite in various proportions can cover the full range of observed magma evolution in Kula

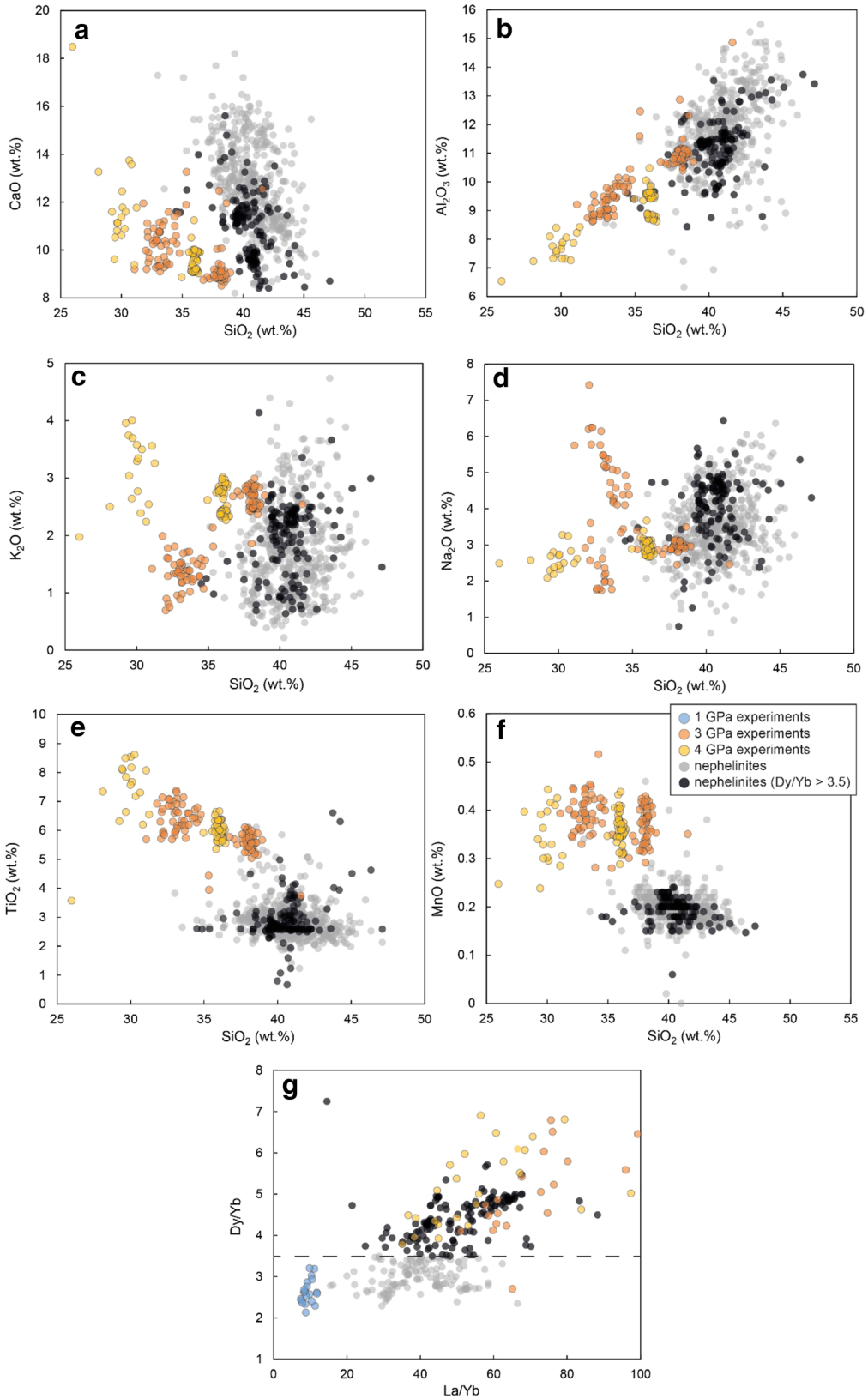
a
CaO (wt.%)
SiO2 (wt.%)
b
Al2O3 (wt.%)
SiO2 (wt.%)
c
K2O (wt.%)
SiO2 (wt.%)
d
Na2O (wt.%)
SiO2 (wt.%)
e
TiO2 (wt.%)
SiO2 (wt.%)
f
MnO (wt.%)
SiO2 (wt.%)
1 GPa experiments
3 GPa experiments
4 GPa experiments
nephelinites
nephelinites (Dy/Yb > 3.5)
g
Dy/Yb
La/Yb

◂**Fig. 12** Major and minor oxide concentration of experimental glasses at 3 GPa (orange) and 4 GPa (yellow). The nephelinites (grey) are taken from a precompiled dataset (DIGIS Team 2022) from the the GEOROC database (https://georoc.eu/). Filtered nephelinites (black) have MgO values between 8 and 15 wt.% and Dy/Yb ratios > 3.5. Experimental glasses overlap nephelinites for most element and oxide concentrations, such as Al_2O_3, MgO, CaO, K_2O, and Na_2O. The experiments have higher TiO_2 and MnO values and slightly lower SiO_2 and FeO concentrations than natural samples

Comparison of the two endmember melts A and B defined by Nikogosian and co-workers with our experiments show that the phonotephritic melt is a good match for endmember A and that the basanitic melt is an excellent match for endmember B for most major, minor, and trace element ratios (Fig. 10). Major and minor element composition of natural Kula lavas and from primitive olivine melt inclusions plot in between experiment E157, which represents melt from low-temperature amphibole breakdown at 1100 °C, and experiments that represent full amphibole melting > 1150 °C (Fig. 10). We argue that the differentiation trend of Kula lavas is not a trend of magma evolution from SiO_2-poor to SiO_2-richer melts, but a mixing line of the two amphibole-related melts (Fig. 11). This is also in good agreement with (1) the lack of any magma chamber that allows larger volumes of magma to differentiate (Saunders et al. 1998), (2) a rather fast ascension rate of Kula lavas, (3) the presence of ultramafic kaersutite-diopside metasome xenoliths in rather evolved phonotephrites, (4) and with the evidence for magma mixing recorded by multiple zoned clinopyroxene phenocrysts that are very common in the Kula lavas (Grützner et al. 2013).

Implications for alkaline volcanism from 3 and 4 GPa experiments

Experimental melts at 3 and 4 GPa are nepheline-normative and plot in the foidite field in Fig. 6. As stated above, experiments at 4 GPa are not necessarily reproducing natural systems and especially this metasome starting material which is naturally amphibole-rich and phlogopite-free argues against a formation at such high pressure. However, amphibole can be stable at 3 GPa and therefore we compare the experiments to a worldwide nephelinite dataset with 2270 entries from the GEOROC database (DIGIS Team 2022). Two filters were applied to the dataset in Fig. 12: (1) only primitive nephelinites with MgO values between 8 and 15 wt.% are taken into account; (2) a threshold of Dy/Yb > 3.5 indicates melt generation in the garnet pressure–temperature stability field. At high-pressure melting (3–4 GPa) garnet is stable in the residuum. Heavy rare earth elements (HREE) like ytterbium are slightly compatible in garnet whereas lighter REE are less compatible. A high Dy/Yb in the melt is, therefore, a good indicator for garnet in the residuum. We found garnet in all 3 and 4 GPa experiments and calculated Dy/Yb ratios > 3.7, whereas at 1 GPa no garnet is present in the experimental residue and Dy/Yb is < 3.2 (Fig. 12).

The remaining list of samples from the reduced nephelinite dataset is small with only 142 entries (6.2% of the full GEOROC dataset) but it shows that the experimental glasses overlap nephelinites for most element and oxide concentrations, such as Al_2O_3, MgO, CaO, K_2O, and Na_2O. The experiments have higher TiO_2 and MnO values and slightly lower SiO_2 and FeO concentrations. Trace elements in nephelinites agree well with the experiments (Fig. 4) but are somewhat less depleted in HREE.

As the oxide concentrations from experiments and natural nephelinites do not fit for elements like SiO_2, TiO_2, and MnO, the composition of natural metasomes must be slightly different at 3 and 4 GPa. It is also likely that amphibole metasomes vary in their composition: Even within the Kula volcanic province, the amphibole-clinopyroxene metasome composition can vary between 42.2 and 37.1 wt.% for SiO_2, or 4.3 and 2.7 wt.% for TiO_2 (Grützner et al. 2013). However, the melting is triggered by amphibole±pyroxene melting and e.g., the kaersutite-diopside metasomes from the Kula volcanic province and clinopyroxene-hornblendites from the French Pyrenees (Pilet et al. 2008) are very similar in composition (44.1 ± 0.1 wt.% SiO_2, 3.63 ± 0.06 wt.% TiO_2 for clinopyroxene hornblendites). With increasing pressure, the melting changes from amphibole melting to phlogopite melting. Phlogopite in our 3 and 4 GPa experiments contains e.g., more K_2O and less CaO, but shows not much difference for SiO_2, TiO_2 or MnO (Table 3).

Alternatively, the nephelinite glasses from the dataset might not represent primary melts and have either reacted with the surrounding mantle rock or differentiated slightly. Increasing SiO_2 concentration and decreasing TiO_2 and MnO values are common trends during magma differentiation.

Finally, it should be considered that most of the natural rock data are from oceanic islands and therefore from below a thin lithosphere. Lloyd and Bailey (1975) have shown that phlogopite is the dominant hydrated phase in the thickened lithosphere, whereas amphibole is present in more thinned regions. This means that even for a compositional overlap between experimental and natural data, it is very unlikely that these natural melts are derived from metasome melting.

Conclusions

- We present a new experimental dataset with reaction experiments between natural amphibole-rich metasomes from the Kula volcanic province and synthetic lherzolite. The melts generated in these experiments range from foidite to phonotephrite over a pressure range of 1–4 GPa and 1100–1300 °C. All melts are alkaline and nepheline-

normative, and their chemical compositions are in good agreement with clinopyroxene-hornblendite melts from Pilet et al. (2008) and expand the dataset of experimental metasome melts to higher pressures.

- At 1 GPa and $T > 1100$ °C, the composition of our melt is controlled by amphibole melting and generates basanites. Between 1000 and 1100 °C amphibole is not stable, but amphibole decompression-breakdown products generate phonotephritic melt.
- At 3 and 4 GPa, phlogopite is stable subsolidus as an additional volatile-bearing mineral phase. Garnet remains in residue during melting together with olivine and clinopyroxene. The change in residual mineral composition generates SiO_2-poor foidite compositions. The residues of both the metasome and the lherzolite transform into wehrlite. Our experiments show that wehrlite formation in the garnet stability field does not require a separate metasomatic process and may be a direct consequence of alkaline melt generation in the mantle.
- We applied a metasome melting model to the magmas of the Kula volcanic province and show that 1 GPa basanite melts and 1 GPa phonotephrite melts cover the range of known Kula lava composition. We argue that the Kula lava compositional trend can be therefore interpreted not as differentiation of asthenospheric basanite but as metasome-driven basanite-phonotephrite mixing. Moreover, the experimental basanite and phonotephrite melts fit chemically to the two melt endmembers that were observed in primitive olivine melt inclusions.
- A comparison of 3 and 4 GPa melts with global nephelinite data shows overlap with most elements but suggest also that the natural nephelinite data do not represent primary melts.

Supplementary Information The online version contains supplementary material available at https://doi.org/10.1007/s00410-023-02052-6.

Acknowledgements This work was partially supported by the Deutsche Forschungsgemeinschaft (DFG). Tobias Grützner is grateful for an EU Marie Skłodowska-Curie Fellowship "ExCliso" (Project ID 101017762). Dejan Prelević was supported through the DFG project PR 1072/9-1. This work has benefited from discussions with Greg Yaxley. We thank the Editor Othmar Müntener and the reviewer Sébastien Pilet for all their comments that helped to improve the manuscript. We also thank the excellent workshops of the Institute for Mineralogy in Münster, especially Maik Trogisch for the sample preparation, and Beate Schmitte for her superb help with EPMA and LA-ICP-MS analyses.

Author Contributions Tobias Grützner: Conceptualization, Experimental investigation, Data acquisition, Validation, Visualization, Writing – original draft, Funding acquisition. Dejan Prelević: Conceptualization, Validation, Writing – review & editing. Jasper Berndt: Data acquisition, Writing – Review & Editing. Stephan Klemme: Funding acquisition, Writing – Review & Editing.

Funding Open Access funding enabled and organized by Projekt DEAL.

Data availability All data of this study are stored in the electronic supplementary material.

Conflict of interest The authors declare that they have no known competing financial interests or personal relationships that could have appeared to influence the work reported in this paper.

References

Artemieva IM, Shulgin A (2019) Geodynamics of Anatolia: lithosphere thermal structure and thickness. Tectonics 38:4465–4487. https://doi.org/10.1029/2019TC005594

Aldanmaz E (2002) Mantle source characteristics of alkali basalts and basanites in an extensional intracontinental plate setting, Western Anatolia, Turkey: Implications for Multi-Stage Melting. Inter Geol Rev 44:440–457. https://doi.org/10.2747/0020-6814.44.5.440

Aldanmaz E, Pickard M, Meisel T, Altunkaynak Ş, Sayıt K, Şen P, Hanan BB, Furman T (2015) Source components and magmatic processes in the genesis of Miocene to Quaternary lavas in western Turkey: constraints from HSE distribution and Hf–Pb–Os isotopes. Contrib Mineral Petrol 170:23. https://doi.org/10.1007/s00410-015-1176-x

Allègre CJ (1982) Chemical geodynamics. Tectonophysics 81:109–132. https://doi.org/10.1016/0040-1951(82)90125-1

Alıcı P, Temel A, Gourgaud A (2002) Pb–Nd–Sr isotope and trace element geochemistry of Quaternary extension-related alkaline volcanism. a case study of Kula region (western Anatolia, Turkey). J Volcanol Geotherm Res 115:487–510. https://doi.org/10.1016/S0377-0273(01)00328-6

Anderson DL (2011) Hawaii, boundary layers and ambient mantle – geophysical constraints. J Petrol 52:1547–1577. https://doi.org/10.1093/petrology/egq068

Chakrabarti R, Basu AR, Ghatak A (2012) Chemical geodynamics of Western Anatolia. Inter Geol Rev 54:227–248. https://doi.org/10.1080/00206814.2010.543787

Daines MJ, Kohlstedt DL (1994) The transition from porous to channelized flow due to melt/rock reaction during melt migration. Geophys Res Lett 21(2):145–148. https://doi.org/10.1029/93GL03052

Dasgupta R, Hirschmann MM (2007) Partial melting experiments of peridotite + CO_2 at 3 GPa and genesis of alkalic ocean island basalts. J Petrol 48:2093–2124. https://doi.org/10.1093/petrology/egm053

Dasgupta R, Hirschmann MM, Smith ND (2007) Water follows carbon: CO_2 incites deep silicate melting and dehydration beneath mid-ocean ridges. Geology 35:135–138. https://doi.org/10.1130/G22856A.1

Davis FA, Hirschmann MM (2013) The effects of K_2O on the compositions of near-solidus melts of garnet peridotite at 3 GPa and the origin of basalts from enriched mantle. Contrib Mineral Petrol 166:1029–1046. https://doi.org/10.1007/s00410-013-0907-0

Davis FA, Hirschmann MM, Humayun M (2011) The composition of the incipient partial melt of garnet peridotite at 3 GPa and the origin of OIB. Earth Planet Sci Lett 308:380–390. https://doi.org/10.1016/j.epsl.2011.06.008

DIGIS Team (2022) "GEOROC Compilation: Rock Types", GRO.data, V4. https://doi.org/10.25625/2jetoa. Accessed September 2022

Dilek Y, Altunkaynak Ş (2010) Geochemistry of Neogene-Quaternary alkaline volcanism in western Anatolia, Turkey, and Implications for the Aegean Mantle. Inter Geol Rev 52:631–655. https://doi.org/10.1080/00206810903495020

Fedorowich JS, Richards JP, Jain JC, Kerrich R, Fan J (1993) A rapid method for REE and trace-element analysis using laser sampling ICP-MS on direct fusion whole-rock glasses. Chem Geol 106(3–4):229–249. https://doi.org/10.1016/0009-2541(93)90029-I

Förster MW, Prelević D, Schmück HR, Buhre S, Veter M, Mertz-Kraus R, Foley SF, Jacob DE (2017) Melting and dynamic metasomatism of mixed harzburgite + glimmerite mantle source: Implications for the genesis of orogenic potassic magmas. Chem Geol 455:182–191. https://doi.org/10.1016/j.chemgeo.2016.08.037

Foley SF (1992) Vein-plus-wall-rock melting mechanisms in the lithosphere and the origin of potassic alkaline magmas. Lithos 28:435–453. https://doi.org/10.1016/0024-4937(92)90018-T

Frey FA, Green DH (1974) Mineralogy, geochemistry and origin of ilherzolite inclusions in Victorian basanites. Geochim Cosmochim Acta 38:1023–1059. https://doi.org/10.1016/0016-7037(74)90003-9

Gervasoni F, Klemme S, Rohrbach A, Grützner T, Berndt J (2017) Experimental constraints on mantle metasomatism caused by silicate and carbonate melts. Lithos 282–283:173–186. https://doi.org/10.1016/j.lithos.2017.03.004

Green DH (1973) Conditions of melting of basanite magma from garnet peridotite. Earth Planet Sci Lett 17:456–465. https://doi.org/10.1016/0012-821X(73)90214-8

Green DH, Ringwood AE (1967) The genesis of basaltic magmas. Contrib Mineral Petrol 15:103–190. https://doi.org/10.1007/BF00372052

Griffin WL, Powell WJ, Pearson NJ, O'Reilly SY (2008) GLITTER: data reduction software for laser ablation ICP-MS. In Sylvester P (ed) Laser Ablation ICP-MS in the Earth Sciences: Current Practices and Outstanding Issues. Mineralogical Association of Canada. Short Course Series 40:308–311

Grützner T, Prelević D, Akal C (2013) Geochemistry and origin of ultramafic enclaves and their basanitic host rock from Kula Volcano, Turkey. Lithos 180–181:58–73. https://doi.org/10.1016/j.lithos.2013.08.001

Grützner T, Kohn SC, Bromiley DW, Rohrbach A, Berndt J, Klemme S (2017) The storage capacity of fluorine in olivine and pyroxene under upper mantle conditions. Geochim Cosmochim Acta 208:160–170. https://doi.org/10.1016/j.gca.2017.03.043

Güleç N (1991) Crust-mantle interaction in western Turkey: implications from Sr and Nd isotope geochemistry of tertiary and quaternary volcanics. Geol Mag 128:417–435. https://doi.org/10.1017/S0016756800018604

Halliday AN, Lee DC, Tommasini S, Davies GR, Paslick CR, Fitton JG, James DE (1995) Incompatible trace elements in OIB and MORB and source enrichment in the sub-oceanic mantle. Earth Planet Sci Lett 133:379–395. https://doi.org/10.1016/0012-821X(95)00097-V

Hart SR (1971) K, Rb, Cs, Sr and Ba contents and Sr isotope ratios of ocean floor basalts. Philos Trans R Soc A 268:573–587. https://doi.org/10.1098/rsta.1971.0013

Heineke C, Niedermann S, Hetzel R, Akal C (2016) Surface exposure dating of Holocene basalt flows and cinder cones in the Kula volcanic field (Western Turkey) using cosmogenic ^{3}He and ^{10}Be. Quat Geochronol 34:81–91. https://doi.org/10.1016/j.quageo.2016.04.004

Hirose K (1997) Partial melt compositions of carbonated peridotite at 3 GPa and role of CO_2 in alkali-basalt magma generation. Geophys Res Lett 24:2837–2840. https://doi.org/10.1029/97GL02956

Hirschmann MM, Stolper EM (1996) A possible role for garnet pyroxenite in the origin of the "garnet signature" in MORB. Contrib Min Petrol 124:185–208. https://doi.org/10.1007/s004100050184

Hirschmann MM, Kogiso T, Baker MB, Stolper EM (2003) Alkalic magmas generated by partial melting of garnet pyroxenite. Geology 31:481–484. https://doi.org/10.1130/0091-7613(2003)031%3c0481:AMGBPM%3e2.0.CO;2

Hofmann AW (1997) Mantle geochemistry: the message from oceanic volcanism. Nature 385:219–229. https://doi.org/10.1038/385219a0

Hofmann AW, White WM (1982) Mantle plumes from ancient oceanic crust. Earth Planet Sci Lett 57:421–436. https://doi.org/10.1016/0012-821X(82)90161-3

Holness MB, Bunbury JM (2006) Insights into continental rift-related magma chambers. Cognate nodules from the Kula Volcanic Province, Western Turkey. J Volcanol Geotherm Res 153:241–261. https://doi.org/10.1016/j.jvolgeores.2005.12.004

Jochum KP, Nohl U, Herwig K, Lammel E, Stoll B, Hofmann AW (2005) GeoReM: a new geochemical database for reference materials and isotopic standards. Geostand Geoanalyt Res 29(3):333–338. https://doi.org/10.1111/j.1751-908X.2005.tb00904.x

Karabulut H, Paul A, Özbakır AD, Ergün T, Şentürk S (2019) A new crustal model of the Anatolia-Aegean domain: evidence for the dominant role of isostasy in the support of the Anatolian plateau. Geophys J Int 218:57–73. https://doi.org/10.1093/gji/ggz147

Kelemen PB, Shimizu N, Salters VJM (1995) Extraction of mid-ocean-ridge basalt from the upwelling mantle by focused flow of melt in dunite channels. Nature 375:747–753. https://doi.org/10.1038/375747a0

Klemme S, Genske F, Sossi PA, Berndt J, Renggli CJ, Stracke A (2022) Cr stable isotope fractionation by evaporation from silicate melts. Chem Geol 610:121096. https://doi.org/10.1016/j.chemgeo.2022.121096

Kogiso T, Hirschmann MM, Frost DJ (2003) High-pressure partial melting of garnet pyroxenite: possible mafic lithologies in the source of ocean island basalts. Earth Planet Sci Lett 216:603–617. https://doi.org/10.1016/S0012-821X(03)00538-7

Kogiso T, Hirschmann MM, Pertermann M (2004) High-pressure partial melting of mafic lithologies in the mantle. J Petrol 45:2407–2422. https://doi.org/10.1093/petrology/egh057

Kunzmann T (1999) The aenigmatite-rhönite mineral group. Eur J Min 11:743–756

Lloyd FE, Bailey DK (1975) Light element metasomatism of the continental mantle: the evidence and the consequences. Phys Chem Earth 9:389–416. https://doi.org/10.1016/0079-1946(75)90030-0

Lundstrom CC, Gill J, Williams Q (2000) A geochemically consistent hypothesis for MORB generation. Chem Geol 162:105–126. https://doi.org/10.1016/S0009-2541(99)00122-9

Lustrino M, Wilson M (2007) The circum-Mediterranean anorogenic Cenozoic igneous province. Earth Sci Rev 81(1-2):1-65. https://doi.org/10.1016/j.earscirev.2006.09.002

Mallik A, Dasgupta R (2012) Reaction between MORB-eclogite derived melts and fertile peridotite and generation of ocean island basalts. Earth Planet Sci Lett 329–330:97–108. https://doi.org/10.1016/j.epsl.2012.02.007

Mahatsente R, Alemdar S, Çemen I (2017) "Effect of slab-tear on crustal structure in Southwestern Anatolia: insight from gravity

data modeling. In neotectonics and earthquake potential of the Eastern Mediterranean Region, Geophysical Monograph Series, American Geophysical Union

Mandler BE, Grove TL (2016) Controls on the stability and composition of amphibole in the Earth's mantle. Contrib Mineral Petrol 171:68. https://doi.org/10.1007/s00410-016-1281-5

Menzies MA, Rogers N, Tindle AG, Hawkesworth CJ (1987) Metasomatic and enrichment processes in lithospheric peridotites, an effect of asthenosphere-lithosphere interaction. In: Menzies MA, Hawkesworth CJ (eds) Mantle metasomatism. Academic Press, London, pp 313–361

Morgan Z, Liang Y (2005) An experimental study of the kinetics of lherzolite reactive dissolution with applications to melt channel formation. Contrib Mineral Petrol 150(4):369–385. https://doi.org/10.1007/s00410-005-0033-8

Niida K, Green DH (1999) Stability and chemical composition of pargasitic amphibole in MORB pyrolite under upper mantle conditions. Contrib Mineral Petrol 135:18–40. https://doi.org/10.1007/s004100050495

Nikogosian IK, Bracco Gartner AJJ, van Bergen MJ, Mason PRD, van Hinsbergen DJJ (2018) Mantle sources of recent Anatolian intraplate magmatism: a regional plume or local tectonic origin? Tectonics 37:4535–4566. https://doi.org/10.1029/2018TC005219

Niu Y, O'Hara MJ (2003) Origin of ocean island basalts: A new perspective from petrology, geochemistry, and mineralphysics considerations. J Geophys Res 108(B4):2209. https://doi.org/10.1029/2002JB002048

Nixon PH (1987) Mantle xenoliths. Wiley, Chichester, p 844

Notsu K, Fujitani T, Ui T, Matsuda J, Ercan T (1995) Geochemical features of collision-related volcanic rocks in central and eastern Anatolia, Turkey. J Volcanol Geotherm Res 64:171–192. https://doi.org/10.1016/0377-0273(94)00077-T

O'Hara MJ (1968) The bearing of phase equilibria studies in synthetic and natural systems on the origin and evolution of basic and ultrabasic rocks. Earth Sci Rev 4:69–133. https://doi.org/10.1016/0012-8252(68)90147-5

Patkó L, Liptai N, Aradi LE, Klébesz R, Sendula E, Bodnar RJ, Kovács IJ, Hidas K, Cesare B, Novák A, Trásy B, Szabó C (2020) Metasomatism-induced wehrlite formation in the upper mantle beneath the Nógrád-Gömör Volcanic Field (Northern Pannonian Basin): evidence from xenoliths. Geosci Front 11:934–964. https://doi.org/10.1016/j.gsf.2019.09.012

Pilet S (2015) Generation of low-silica alkaline lavas: petrological constraints, models, and thermal implications. In: Foulger GR, Lustrino M, King SD (ed) The Interdisciplinary Earth: A Volume in Honor of Don L. Anderson: Geological Society of America Special Paper 514 and American Geophysical Union Special Publication 71, pp 281–304

Pilet S, Baker MB, Stolper EM (2008) Metasomatized lithosphere and the origin of alkaline lavas. Science 320:916–919. https://doi.org/10.1126/science.1156563

Prelević D, Jacob D, Foley SF (2013) Recycling plus: a new recipe for the formation of alpine-Himalayan orogenic mantle lithosphere. Earth Planet Sci Lett 362:187–197. https://doi.org/10.1016/j.epsl.2012.11.035

Prelević D, Akal C, Foley SF, Romer RL, Stracke A, Van Den Bogaard P (2012) Ultrapotassic mafic rocks as geochemical proxies for post-collisional dynamics of orogenic lithospheric mantle: the case of Southwestern Anatolia, Turkey. J Petrol 53:1019–1055. https://doi.org/10.1093/petrology/egs008

Prelević D, Akal C, Romer RL, Mertz-Kraus R, Helvacı C (2015) Magmatic response to slab tearing: constraints from the afyon alkaline volcanic complex, Western Turkey. J Petrol 56(3):527–562. https://doi.org/10.1093/petrology/egv008

Richardson-Bunbury JM (1996) The Kula Volcanic Field, western Turkey: the development of a Holocene alkali basalt province and the adjacent normal-faulting graben. Geol Mag 133:275–283. https://doi.org/10.1017/S0016756800009018

Rudnick RL, McDonough WF, Chappell BW (1993) Carbonatite metasomatism in the northern Tanzanian mantle: petrographic and geochemical characteristics. Earth Planet Sci Lett 114:463–475. https://doi.org/10.1016/0012-821X(93)90076-L

Salaün G, Pedersen HA, Paul A, Farra V, Karabulut H, Hatzfeld D, Papazachos C, Childs DM, Pequegnat C, SIMBAAD Team (2012) High-resolution surface wave tomography of the Aegean-Anatolia region: constraints on upper mantle structure. Geophys J Int 190:406-420. https://doi.org/10.1111/j.1365-246X.2012.05483.x

Saunders P, Priestley K, Taymaz T (1998) Variations in the crustal structure beneath western Turkey. Geophys J Int 134:373–389. https://doi.org/10.1046/j.1365-246x.1998.00571.x

Sharygin VV, Kóthay K, Szabó C, Timina TJ, Török K, Vapnik Y, Kuzmin DV (2011) Rhönite in alkali basalts: silicate melt inclusions in olivine phenocrysts. Russ Geol Geophys 52:1334–1352. https://doi.org/10.1016/j.rgg.2011.10.006

Şen E, Aydar E, Şen P, Gourgaud A (2023) Insight into a rift volcanism with the petrogenesis of ultramafic enclaves and the host basalts: Kula Volcanic Field, Western Anatolia. Turkey Ital J Geosci 142(2):291–315. https://doi.org/10.3301/IJG.2023.16

Shaw CSJ (2009) Textural development of amphibole during breakdown reactions in a synthetic peridotite. Lithos 110:215–228. https://doi.org/10.1016/j.lithos.2009.01.002

Shaw CS, Eyzaguirre J, Fryer B, Gagnon J (2005) Regional variations in the mineralogy of metasomatic assemblages in mantle xenoliths from the West Eifel Volcanic Field, Germany. J Petrol 46(5):945–972. https://doi.org/10.1093/petrology/egi006

Stoll B, Jochum KP, Herwig K, Amini M, Flanz M, Kreuzburg B, Kuzmin D, Willbold M, Enzweiler J (2008) An automated iridium-strip heater for LA-ICP-MS bulk analysis of geological samples. Geostand Geoanalyt Res 32(1):5–26. https://doi.org/10.1111/j.1751-908X.2007.00871.x

Straub SM, LaGatta AB, Martin-Del Pozzo AL, Langmuir CH (2008) Evidence from High-Ni Olivines for a Hybridized Peridotite/pyroxenite Source for Orogenic Andesites from the Central Mexican Volcanic Belt. Geochem Geophys Geosys 9:Q03007. https://doi.org/10.1029/2007GC001583

Takahashi E (1986) Melting of a dry peridotite KLB-1 up to 14 GPa – Implications on the origin of peridotitic upper mantle. J Geophys Res 91:9367–9382. https://doi.org/10.1029/JB091iB09p09367

Tokçaer M, Agostini S, Savaşçın MY (2005) Geotectonic setting and origin of the youngest Kula volcanics (Western Anatolia), with a new emplacement model. Turk J Earth Sci 14:145–166

Van den Bleeken G, Müntener O, Ulmer P (2010) Reaction processes between tholeiitic melt and residual peridotite in the uppermost mantle: an experimental study at 0·8 GPa. J Petrol 51(1–2):153–183. https://doi.org/10.1093/petrology/egp066

Van den Bleeken G, Müntener O, Ulmer P (2011) Melt variability in percolated peridotite: an experimental study applied to reactive migration of tholeiitic basalt in the upper mantle. Contrib Mineral Petrol 161:921–945. https://doi.org/10.1007/s00410-010-0572-5

Walters JB (2022) MinPlot: A mineral formula recalculation and plotting program for electron probe microanalysis. Mineralogia 53/1:51–66. https://doi.org/10.2478/mipo-2022-0005

Wang J, Xiong X, Zhang L, Takahashi E (2020) Element loss to platinum capsules in high-temperature-pressure experiments. Am Mineral 105:1593–1597. https://doi.org/10.2138/am-2020-7580

Wasylenki LE, Baker MB, Kent AJR, Stolper EM (2003) Near-solidus melting of the shallow upper mantle: partial melting experiments on depleted peridotite. J Petrol 44:1163–1191. https://doi.org/10.1093/petrology/44.7.1163

Wilson M, Downes H, Cebria JM (1995) Contrasting fractionation trends in coexisting continental alkaline magmas series: Cantal, Massif Central, France. J Petrol 36:1729–1753. https://doi.org/10.1093/oxfordjournals.petrology.a037272

Yaxley GM, Crawford AJ, Green DH (1991) Evidence for carbonatite metasomatism in spinel peridotite xenoliths from western Victoria, Australia. Earth Planet Sci Lett 107:305–317. https://doi.org/10.1016/0012-821X(91)90078-V

Yaxley GM, Green DH, Kamenetsky V (1998) Carbonatite metasomatism in the southeastern Australian lithosphere. J Petrol 39(11–12):1917–1930. https://doi.org/10.1093/petroj/39.11-12.1917

Zindler A, Hart S (1986) Chemical geodynamics. Annu Rev Earth Planet Sci 14:493–571. https://doi.org/10.1146/annurev.ea.14.050186.002425

Zinngrebe E, Foley SF (1995) Metasomatism in mantle xenoliths from Gees, West Eifel, Germany: evidence for the genesis of calc-alkaline glasses and metasomatic Ca-enrichment. Contrib Mineral Petrol 122(1–2):79–96. https://doi.org/10.1007/s004100050114